Feature

Wireless LAN Comes of Age: Understanding the IEEE 802.11n Amendment

Thomas Paul and Tokunbo Ogunfunmi

Abstract

During the initial development of the IEEE 802.11n (11n) amendment for improving the throughput of wireless LANs, a lot of excitement existed surrounding the potential higher throughput (i.e., faster downloads), and increased range (distance) achievable. However, delays in the development of this standard (which began in 2003, and is still in the final draft stages) as well as vendor, customer reluctance to adopt the pre-11n offerings in the marketplace, have generally slowed interest in this next-generation technology.

However, there is still much to be excited about. The latest draft of IEEE 802.11n (Draft 3.0) offers the potential of throughputs beyond 200 Mbps, based on physical layer (PHY) data rates up to 600 Mbps. This is achieved through the use of multiple transmit and receive antennas, referred to as MIMO (multiple input, multiple output). Using techniques such as spatial division multiplexing (SDM), transmitter beamforming, and space-time block coding (STBC), MIMO is used to increase dramatically throughput over single antenna systems (by two to four times) or to improve range of reception, depending on the environment.

This article offers an exposition on the techniques used in IEEE 802.11n to achieve the above improvements to throughput and range. First, the current generation WLAN devices (11a/b/g) are described in terms of the benefits offered to end users. Next, the evolution of the 11n amendment is discussed, describing the main proposals given, and illustrating reasons for the delay in standardization. Then, the changes to the PHY for 11n are presented. A description of channel modeling with MIMO is shown, followed by the signal processing techniques employed, including MIMO channel estimation and detection, space-time block coding (STBC), and transmitter beamforming. Simulation results are presented which illustrate the benefits of these techniques, versus the existing 11a/g structures, for both throughput and range. Finally, a brief section outlining considerations for the rapid prototyping of a baseband design based on the 802.11n PHY is presented. We conclude with a discussion of the future for 11n, describing the issues addressed with Drafts 2.0 and 3.0, as well as its place in a wireless market with WiMAX and Bluetooth.

Digital Object Identifier 10.1109/MCAS.2008.915504

 1531-636X/08/$25.00©2008 IEEE

I. Introduction

The IEEE 802.11n amendment is the latest addition under development for the IEEE 802.11 standard providing a marked increase in throughput (from 20 Mbps to around 200 Mbps, in practice) as well as range of reception (through reducing signal fading) over the IEEE 802.11a/g standards currently in use. Multiple antennas, or MIMO (Multiple-Input, Multiple-Output), is the key innovation used to obtain these benefits.

The current draft for the IEEE 802.11n amendment supports the use of MIMO features such as spatial-division multiplexing (SDM), space-time block coding (STBC) and transmitter beamforming. In addition, there are provisions for the use of advanced coding with LDPC (low-density parity check codes), as well as a 40 MHz bandwidth mode (known as channel bonding). The above features allow the IEEE 802.11n amendment to specify data rates up to 600 Mbps, a more than ten-fold increase over the maximum data rate with the 11a/g standards.

The focus of this article is to explore the techniques used in the IEEE 802.11n amendment to achieve these improvements to range and throughput. A history of the IEEE 802.11 standard is presented first, setting up a discussion on the evolution of the 802.11n amendment, where the main proposals are outlined. Afterwards, the physical layer (PHY) for 802.11n is described. Channel modeling under MIMO is shown first, followed by the MIMO processing techniques used in extending the throughput and range, including: MIMO channel estimation and detection, space-time block coding (STBC), and transmitter beamforming.

Thomas Paul and Tokunbo Ogunfunmi are with the Department of Electrical Engineering, Santa Clara University, Santa Clara, CA 95053. E-mail: togunfunmi@scu.edu.

Simulation results showing the benefits of the above techniques for the IEEE 802.11n standard are provided, and the results compared with those of the existing 11a/g standard, for both throughput and range. Finally, a discussion of hardware prototyping issues as well as future trends for IEEE 802.11n are presented, in terms of the issues addressed with Drafts 2.0 and 3.0, in addition to how the IEEE 802.11n standard co-exists (in terms of both interoperability, as well as strategically) in a market with Bluetooth and WiMAX.

II. History of IEEE 802.11 Standard to Date

With the emergence of high-speed internet connections such as DSL and cable modems in the 1990's (which provide data rates of several Mbps, compared to the 56 Kbps rates for dial-up modems), as well as the popularity of notebook computers at the office, a large interest in providing high-speed wireless network access emerged [1]. Initially, many companies started developing wireless products trying to achieve this. However, these products suffered from many issues, including high manufacturing costs and low production volume, as well as product incompatibility between vendors [2]. The IEEE 802.11 standard was developed in an effort to resolve these issues.

The original IEEE 802.11 standard was completed in 1997. It provided three initial specifications for the physical layer (PHY) [3]. Two of the three specifications described radio-based PHYs with a 2.4 GHz carrier. The first was a frequency hopping spread spectrum (FHSS) PHY. The other was a direct-sequence spread spectrum (DSSS) PHY. Finally, an infra-red (IR) PHY, operating at baseband, was also described.

The above PHY layers were all designed to support 1Mbps (Megabits per second) and 2Mbps rates. The two radio-based PHYs were both specified for operation at 2.4 GHz, which is part of the unlicensed frequency range known as the ISM (Industrial, Scientific, and Medical) band [1], [2]. Although this frequency range is unlicensed (i.e., an FCC license is not required for its use), this makes the frequency range attractive to the developers of other systems as well, leading to interference between competing (and unlicensed) services in this band (i.e., Bluetooth, WiMAX). This issue is discussed in more detail towards the end of this article.

By 1999, two amendments were added to the IEEE 802.11 standard. The IEEE 802.11b (11b) amendment described an extension to the previously-defined PHY with DSSS, providing additional data rates up to 11 Mbps, using a modulation scheme known as complementary-code keying (CCK). Meanwhile, the other amendment, IEEE 802.11a (11a), specified a new radio-based PHY at 5.2 GHz using a transmission scheme known as Orthogonal Frequency-Division Multiplexing (OFDM) allowing for rates up to 54 Mbps. Note that, although 802.11b may appear to be the older standard (based on the older PHY, and since 11a products were introduced after 11b), the amendment for 802.11a was actually proposed before 802.11b.

Although the IEEE 802.11b PHY is capable of 11 Mbps, the throughput achieved, in practice, does not exceed 5 Mbps (due to packet overhead, delays, etc.) which is insufficient for many (in particular, video-based) applications. Thus, interest grew in developing IEEE 802.11a products, which were capable of providing throughputs above 20 Mbps (i.e., about half the 54 Mbps PHY data rate).

However, the IEEE 802.11a standard suffered from the fact that it described the use of a 5.2 GHz carrier for the PHY. Although this allows for the coexistence of 11b and 11a networks without 'over-the-air' interference, the production cost of manufacturing devices capable of supporting both 2.4 GHz and 5.2 GHz (to support both standards) became a barrier preventing the transition from 802.11b to 802.11a products in the marketplace. In addition, the use of 5.2 GHz carrier in Europe was generally restricted, making IEEE 802.11a popular only in North America.

To resolve these problems, the IEEE 802.11g standard was developed. This standard defines a PHY layer with similar specifications to IEEE 802.11a (use of OFDM, PHY rates up to 54 Mbps), but based on a 2.4 GHz carrier. The main challenges in the development of this standard mostly involved ensuring backwards compatibility with the IEEE 802.11b standard (in particular, allowing 11b devices to join 11g networks).

Although IEEE 802.11g provides good performance for most user needs, some possible usage models, such as the support of simultaneous, high-quality video streaming for multiple users (for example, establishing multiple video-conferencing sessions on one WLAN network) can lead to an interest in providing gigabit-type throughputs with wireless LAN. The IEEE 802.11n standard brings us closer towards this goal, in addition to improving range of operation and quality-of-service (QoS).

Development of the IEEE 802.11n amendment to the standard began in late 2003, when the IEEE (Institute of Electrical and Electronics Engineers) formed the TGn task group to start work on the specification. Initially, the goal was to allow rates of at least 100 Mbps, essentially doubling the existing maximum rate of 54 Mbps for the 802.11a/g specifications. Initially, many hardware and networking companies had suggestions for this new amendment, resulting in as many as 61 proposals being submitted to the IEEE [4]. By February, 2005, however, these draft proposals were narrowed down to two, both with strong backing from various companies.

One was a proposal by the WWiSE (World Wide Spectrum Efficiency) group, which included companies such as Airgo Networks, Broadcom, Motorola, and Texas Instruments. This proposal suggested the use of channels with similar bandwidth to the existing 11b/g networks (20 MHz) as well as the use of multiple transmit and receive antennas, or MIMO, to achieve throughput rates of around 135 Mbps in real-world conditions.

The other proposal was by the TGn Sync group, which consisted of Atheros Communications, Intel, Philips, Sony, among others. The proposal suggested doubling the bandwidth to 40 MHz, to essentially double the throughput. In addition, other, more sophisticated processing techniques allowed the TGn Sync devices to transmit data at rates up to 315 Mbps.

The two proposals evolved over the next couple of months to form the main competing proposals for IEEE 802.11n standard. Both offered provisions for MIMO communications with up to four transmit antennas, and four receive antennas. Both supported an optional 40 MHz bandwidth mode. The two proposals also differed in areas such as data interleaving, space-time coding, and channel estimation approaches. The TGn Sync proposal also has additions for transmit beamforming and spatial spreading.

Due to the significant support each proposal enjoyed, neither proposal was able to obtain the majority vote required for adoption toward the IEEE 802.11n standard.

Finally, in July 2005, a group consisting of members of both proposal groups agreed to form a joint proposal group, which submitted a new proposal to the TGn workgroup in January 2006. This proposal, referred to as the TGn Joint proposal, combined the benefits of the other proposals, and formed the basis of the current drafts for the 802.11n standard.

III. Modifications to 802.11 Standard with 11n Amendment

To achieve the increased throughput and range envisioned for IEEE 802.11, the 11n amendment describes enhancements to both the physical (PHY) and medium access control (MAC) layers. Modifications to the MAC include the addition of frame aggregation (i.e., sending multiple MAC frames in one PHY layer packet to reduce overhead), block ACK enhancements (acknowledging frames in blocks, also to reduce overhead), a reverse-direction (RD) protocol (allows the transmit station currently holding the air channel to efficiently transfer control to another station, without the need for the other station to initiate a data transfer) as well as schemes for co-existence with legacy devices.

Other modifications include:

- Quality of Service (QoS) features, to support delay-sensitive applications such as Voice over WLAN (VoWLAN) and multimedia streaming (described in 802.11e),
- power save multi-poll (or PSMP) feature, a battery saving feature for WLAN in handheld devices,
- extended channel switch announcement, i.e., allowing an Access Point (AP) to switch between support of 20 MHz only, and 20 MHz/40 MHz (described in 802.11y),
- improved radio resource management, i.e., efficient use of multiple APs within a network (described in 802.11k),
- support for fast roaming, i.e., fast handoffs between base stations, intended for use in supporting mobile phones using VoIP and wireless networks instead of cellular networks (described in 802.11r).

Details of the above changes can be found in [5], as well as the other amendments. Regarding frame aggregation, the reader can refer to [6] for a discussion of its required use for achieving throughputs beyond 100 Mbps (the initial goal of the 11n amendment).

The focus of this section, however, is on the modifications to the PHY layer, which include:

- Use of multiple transmit and receive antennas (known as MIMO),
- Channel bonding (i.e., use of two 20 MHz bandwidth streams),
- Advanced coding (i.e., low-density parity check, or LDPC, codes).

In this article, we emphasize the use of MIMO techniques. First, we consider how the indoor wireless channel can be modeled under MIMO. Afterwards, the main MIMO techniques for achieving the desired throughput and range benefits are described.

Figures 1 and 2 show block diagrams of general MIMO transmit and receive datapath structures for an IEEE 802.11n PHY. The purpose of the key modules shown in these figures should become clear by the end of this section. The reader may also refer to [5], [7]–[10] for details of the MIMO datapath.

III.1 Channel Modeling with MIMO

In this sub-section, we present a description for the modeling of indoor wireless channels under MIMO. The single antenna case (i.e., the channel from a single transmit antenna to a single receive antenna) can be seen as a subset of MIMO. The goal in illustrating the MIMO channel model is to aid the understanding of the characteristics of the wireless environment, as well as the MIMO techniques shown later.

For wireless channel modeling, the two key signal propagation models are:

- Large-scale propagation (also known as large-scale path loss),

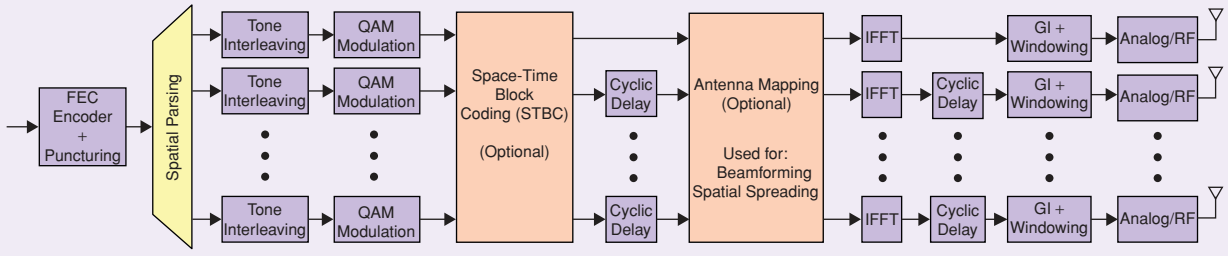

Figure 1. General MIMO TX Datapath.

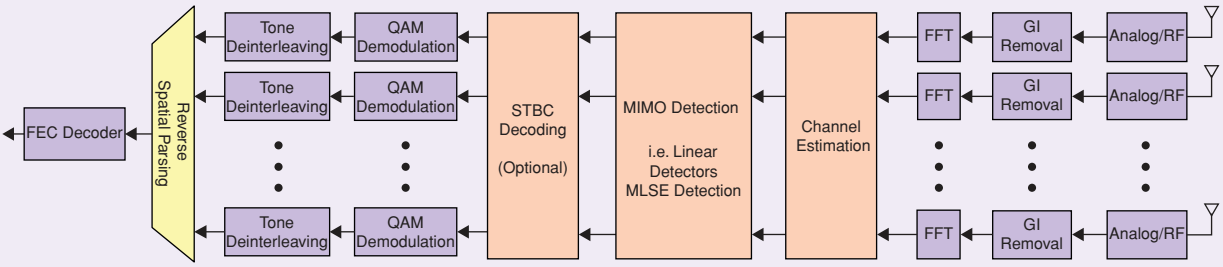

Figure 2. General MIMO RX Datapath.

- Small-scale propagation (also known as small-scale fading).

The above two forms of signal propagation are described below. Note, however, that the physics in determining precise propagation models can become rather complex (i.e., involves studying the propagation of electromagnetic waves considering various effects such as signal reflection, diffraction, and scattering as well as the location, motion, and material composition of surrounding objects [1], [11]). The focus instead is on providing statistical models suitable for describing the received signal after propagation through typical indoor environments.

The descriptions to follow are based on the TGn channel models [7], which were developed by the TGn workgroup to provide sufficient channel models for IEEE 802.11n PHY layer simulation and performance testing. In addition to [7], detailed descriptions of both large-scale path loss and small-scale fading can be found in [1], [2], [11].

III.1.1 Large-Scale Path Loss

Large-scale path loss refers to the average loss in signal strength over distance. For indoor environments, the path loss differs at close range (around 5 to 10 meters), compared to larger distances. These short distances are considered free space (i.e., open space with no path reflections). For larger distances, path reflections from the environment (especially reflections from surrounding walls) generally result in a steeper overall drop in signal strength at the receiver.

Figure 3 illustrates path loss over distance (plotted in log scale) for an indoor environment.

The path loss occurring in free space, larger distances, can generally be modeled as follows:

$$\begin{aligned} L(d) &= L_{FS}(d), && d \le d_{BP} \\ L(d) &= L_{FS}(d_{BP}) + 3.5 \cdot 10 \log_{10}(d/d_{BP}), && d > d_{BP} \end{aligned} \quad (1)$$

where the first equation gives the path loss (in decibels, or dB) for free space (distances less than d_{BP}, known as the breakpoint distance), and the second equation gives the path loss beyond distance d_{BP}.

The term $L_{FS}(.)$ refers to the free space path loss equation. This expression applies to distances less than d_{BP} (as stated previously) and has a slope of 2 (in dB scale). The expression for free space path loss, $L_{FS}()$ is, from [11]:

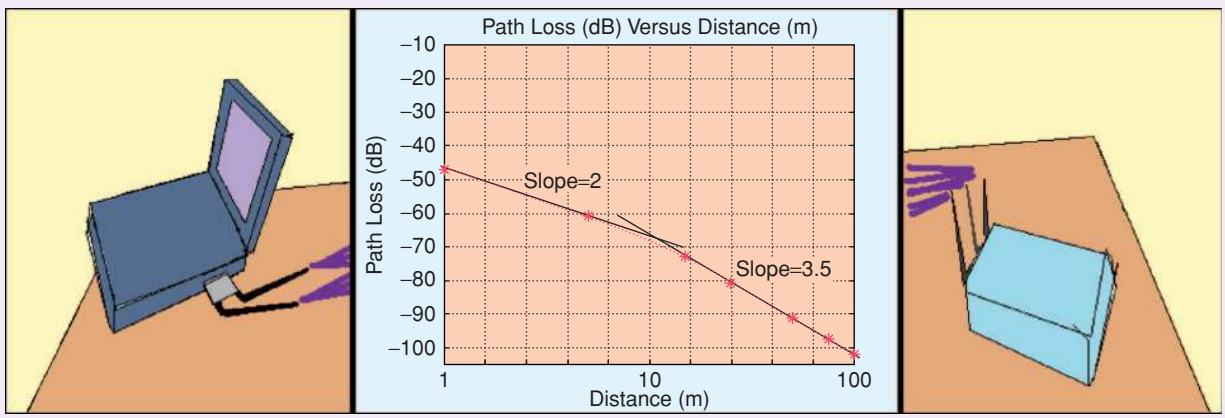

Figure 3. Illustration of path loss.

Table 1.
Path Loss Parameters for TGn Channel Models (reprinted from [7]).

New Model	d_{BP} (m)	Slope Before d_{BP}	Slope After d_{BP}	Shadow Fading std. dev. (dB) Before d_{BP} (LOS)	Shadow Fading std. dev. (dB) After d_{BP} (NLOS)
A (Optional)	5	2	3.5	3	4
B	5	2	3.5	3	4
C	5	2	3.5	3	5
D	10	2	3.5	3	5
E	20	2	3.5	3	6
F	30	2	3.5	3	6

$$L_{FS}(d) = -10 \log_{10}\left(\frac{G_t G_r \lambda^2}{(4\pi d)^2}\right) \tag{2}$$

where G_t, G_r are the transmitter and receiver antenna gains, respectively, d is the distance between them, in meters (known as T-R separation [11]), and λ is the wavelength of the transmitted carrier frequency. Assuming unity antenna gains ($G_t = G_r = 1$), equation (2) can be written as (with carrier frequency, $f_c = 5.25$ GHz):

$$\begin{aligned} L_{FS}(d) &= 10 \log_{10}\left(\frac{(4\pi d)^2}{\lambda^2}\right) \\ &= 2 \cdot 10 \log_{10}(4\pi/\lambda) + 2 \cdot 10 \log_{10}(d) \\ &= 47\,dB + 2 \cdot 10 \log_{10}(d) \end{aligned} \tag{3}$$

Note that the slope is 2 for the path loss expression in (3). For distances larger than d_{BP}, the slope is 3.5, which can be seen from (1). The parameters used to model path loss for the different TGn channel models in [7] are shown below. Note that channel models A to C represent small environments (0 to 30 ns delay spread), and models D to F represent larger environments (50 to 150 ns delay spread):

The shadow fading values in Table 1, above, represent the fact that, for any given transmitter/receiver configuration, the regions surrounding these stations can differ, resulting in the received signal having an average strength differing from (1). From [11], this configuration-dependent variation in path loss (known as shadow fading, or log-normal shadowing) can be modeled with a zero-mean, Gaussian random variable, with standard deviation, σ (in dB), added to the path loss.

With shadow fading added to (1), the equations become:

$$\begin{aligned} L(d) &= L_{FS}(d) + X_\sigma, && d \le d_{BP} \\ L(d) &= L_{FS}(d_{BP}) + 3.5 \cdot 10 \log_{10}(d/d_{BP}) + X_\sigma, && d > d_{BP} \end{aligned} \tag{4}$$

where X_σ is the random variable described above. Note that the value for σ differs before and after the breakpoint distance (see Table 1), and that the breakpoint distance is generally assumed to be the boundary for LOS (Line-Of-Sight) conditions [7].

The table below shows the computed path loss for various distances with TGn Channel D, based on the above described model, as well as the expected average SNR at the receiver, assuming the transmit station uses +5 dBm transmit power, and the receive station has a −90 dBm receive sensitivity (or signal detection threshold), with no external interference.

III.1.2 Small-Scale Signal Fading

Small-scale fading are fading effects caused by small changes in distance (only a few wavelengths). These fading effects are caused by multiple reflected

Table 2.
Path Loss, SNR, at various distances for TGn Channel D.

Distance	Path Loss	SNR
1 m (3 ft)	47.0 dB	48.0 dB
3 m (10 ft)	56.5 dB	38.5 dB
6 m (20 ft)	62.5 dB	32.5 dB
9 m (30 ft)	66.0 dB	29.0 dB
12 m (40 ft)	70.0 dB	25.0 dB
15 m (50 ft)	73.0 dB	22.0 dB
18 m (60 ft)	76.0 dB	19.0 dB
...	...	...
30 m (100 ft)	84.0 dB	11.0 dB
...	...	...
46 m (150 ft)	90.0 dB	5.0 dB
...	...	...
55 m (180 ft)	93.0 dB	2.0 dB

versions of the transmitted signal combining, at the receiver, in either a constructive or destructive fashion. Note that these effects generally dominate the performance of the receiver (compared to large-scale path loss), since they vary dramatically over short distances and periods of time [11].

To provide some basic intuition for the small-scale signal fading effects under MIMO, consider the structure illustrated in Figure 4 (the reader is encouraged to consider more exotic cases, i.e., various objects and reflection paths, to convince themselves of the intuition to follow).

Considering Figure 4, we make two observations:

1) the channel response from any transmit antenna, j, to any receive antenna, i, is the sum of various reflection paths. Since these paths can have different propagation delays (delays in the arrival times), the impulse response can have a large spread across time.
2) the overall received signal for each receive antenna is the sum of the signals from all transmit antennas (with channel applied).

Based on the above, the MIMO channel can be written as [12]:

$$r(t) = \sum_{k=-\infty}^{\infty} H(t - kT)a(k) + n(t) \tag{5}$$

with:

$$H(\tau) = \begin{bmatrix} h_{1,1}(\tau) & \cdots & h_{1,M}(\tau) \\ \vdots & \ddots & \vdots \\ h_{N,1}(\tau) & \cdots & h_{N,M}(\tau) \end{bmatrix}$$

$$a(k) = \begin{bmatrix} a_1(k) \\ \vdots \\ a_M(k) \end{bmatrix} \quad n(t) = \begin{bmatrix} n_1(t) \\ \vdots \\ n_N(t) \end{bmatrix} \tag{6}$$

where:

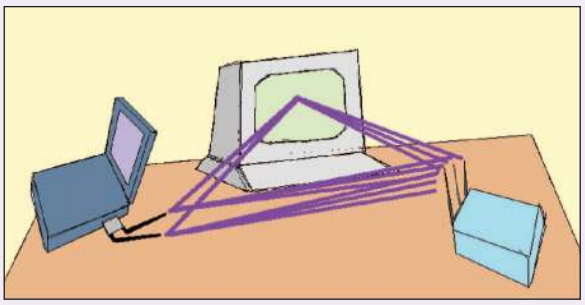

Figure 4. Example of a MIMO channel.

- $H(\tau)$ is the time-domain MIMO channel,
- $\boldsymbol{a}$ is the transmitted sequence (with each element $a(k)$ being a vector across transmit streams),
- T is the time interval between each element $a(k)$ in the transmitted sequence, and
- $n(t)$ is a noise vector.

Equations (5) and (6) also assume M transmit streams and N receive antennas. In addition, each element $h_{i,j}(\tau)$ in matrix $H(\tau)$ is the channel impulse response from transmit data stream, j, to receive antenna, i. Note, however, that each channel response $h_{i,j}(\tau)$ may also be time-varying, since the transmitting and receiving stations as well as surrounding objects may be in motion.

In general, each element $h_{i,j}(\tau)$ in matrix $H(\tau)$ can be expressed as [13]:

$$h(\tau, t) = \sum_n \alpha_n(t) e^{-j2\pi f_c \tau_n(t)} \delta(\tau - \tau_n(t)) \tag{7}$$

where the sub-indices i and j were removed for convenience of notation, and parameter t was added to represent the time-varying nature of the channel (i.e., the time index where channel was sampled). In addition:

- τ is the delay index of channel response (i.e., channel response at time: $t - \tau$),
- n is the index of the reflection path for transmit stream, j, to receive antenna, i,
- $\alpha_n(t)$ is the channel attenuation over path n at time t,
- $e^{-2\pi \cdots}$ represents the carrier phase offset between the transmitting, receiving stations due to path delay τ_n,
- $\delta(t - \tau_n(t))$ represents the propagation delay of the transmitted signal over a particular path n.

Since the proper reception of WLAN packets requires a time-invariant channel, WLAN packets are designed to have short time durations, where the channel is said to experience quasi-static fading, i.e., channel fading is constant for each block (packet), but can change independently for each block [14]. With this change, the time index t, can be removed from the channel response expression:

$$h(\tau) = \sum_n \alpha_n e^{-j2\pi f_c \tau_n} \delta(\tau - \tau_n) \tag{8}$$

To determine an appropriate packet duration which allows the channel to remain time-invariant, consider that the channel response is time-varying due to motion of objects, which typically occurs at walking speeds, approximately 1.2 km/h (0.333 m/s) for indoor environments [7].

Although motion results in a change in the reflection paths from the transmitting to receiving antennas (thus changing the $h_{i,j}(\tau)$ impulse responses), typically the most immediate effect of motion is an amplitude change

(i.e., gain or fade) of the received signal, resulting from the shift in carrier phase for the RF signal. This effect is described below.

If we consider the wavelength (or distance the RF signal travels before the carrier phase changes by 2π):

$$\lambda = \frac{c}{f_c} = \frac{3 \times 10^8\, m/s}{5.25 \times 10^9\, Hz} = 0.0571\, m \tag{9}$$

where f_c is carrier frequency (5.25 GHz), and c is speed of the RF signal (approximately the speed of light).

And considering the speed of object motion (max speed: $v_o = 0.333$ m/s):

$$f_d = \frac{v_o}{\lambda} = \frac{0.333\, m/s}{0.0571\, m} = 5.8\, Hz \tag{10}$$

We see the motion results in a worst-case frequency shift of around 5.8 Hz, known as Doppler spread [7]. Figure 5 illustrates the wavelength, Doppler spread parameters.

To determine the time period where the channel remains essentially time-invariant, the reciprocal of Doppler spread is used. This time duration is known as coherence time, which is $T_c = 1/(5.8$ Hz), or 0.172 sec. with the above assumptions.

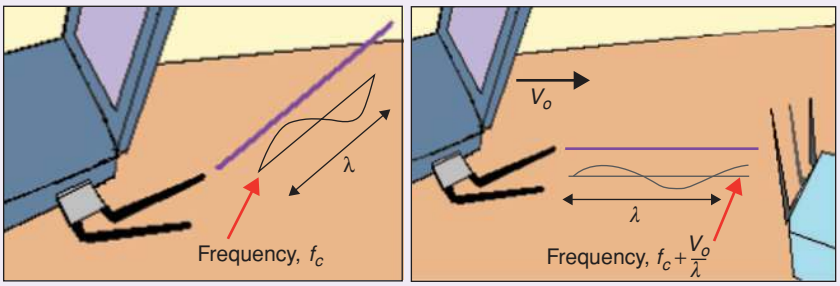

Figure 5. Examples of wavelength, Doppler spread.

Typically, the above formula for coherence time is considered too long. Specifically, it does not consider the significant signal fade that can result with the change in multipath characteristic, due to Rayleigh fading [11]. A better measure is:

$$T_C = \sqrt{\frac{9}{16\pi f_d^2}} = \frac{0.423}{f_d} = \frac{0.423}{5.8\, Hz} = 0.0729\, \text{sec} \tag{11}$$

WLAN packets are typically less than 1 ms (0.001 sec), in the worst case, to prevent time-varying channel response (maintain quasi-static fading).

The channel effects described above (time-varying channel response, Doppler spread) are also known as time-selective fading and frequency dispersion, respectively.

Other small-scale fading effects are based on the fact that the channel response is spread across time. This can be seen from (8) (repeated here for convenience):

$$h(\tau) = \sum_n \alpha_n e^{-j2\pi f_c \tau_n} \delta(\tau - \tau_n) \tag{12}$$

From (8), (12), we can see that the spread of the channel response (known as RMS delay spread) is based on the different propagation delay τ_n of each path n forming the multipath channel response.

Note that RMS delay spread should actually be measured as the square-root of the second moment (variance) of the power delay profile ([11]), which is shorter than the difference between the maximum and minimum path propagation delays. However, the maximum, minimum delay difference is used here for ease of comparison (considered an upper bound for delay spread).

Based on (12), we can see that if the delays are spread widely (known as time dispersion), the transmit symbols become combined after applying convolution with channel (commonly referred to as inter-symbol interference). This results in a frequency response which depends on the past symbols (known as frequency-selective fading). Note that the transmitted data can still be recovered under frequency-selective fading (by considering the channel as a linear filter of past symbols [11]), but the approach leads to a more complex receiver design.

In order to get an idea of the possible worst-case values for delay spread, we consider a large, office-type, indoor environment (length around 100 m).

For the example in Figure 6, we can see that the shortest, line-of-sight (LOS), path is 20 m, while the larger propagation path has a length of: $2\sqrt{75^2 + 10^2} = 151.3\, m$

The propagation delays are:

$$\tau_1 = \frac{d_1}{c} = \frac{20\, m}{3 \times 10^8\, m/s} = 6.67 \times 10^{-8}\, \text{sec} = 66.7\, n\, \text{sec}$$

$$\tau_2 = \frac{d_2}{c} = \frac{151.3\, m}{3 \times 10^8\, m/s} = 50.43 \times 10^{-8}\, \text{sec} = 504.3\, n\, \text{sec} \tag{13}$$

Thus, for the scenario in Figure 6, the delay spread should be less than: $\tau_{ds} = (504.3\text{ ns} - 66.7\text{ ns}) = 437.7$ ns.

With the above delay spread, the channel delay spread leads to inter-symbol interference after convolution with channel. However, with a symbol time significantly larger than this delay spread, the channel appears as a delta function, which results in uniform fading over all frequencies (known as flat fading [11]). This is illustrated in Figure 7.

The relationship between delay spread and flat fading also gives rise to the concept of coherence bandwidth, or the frequency bandwidth where the signal experiences flat fading for a particular delay spread.

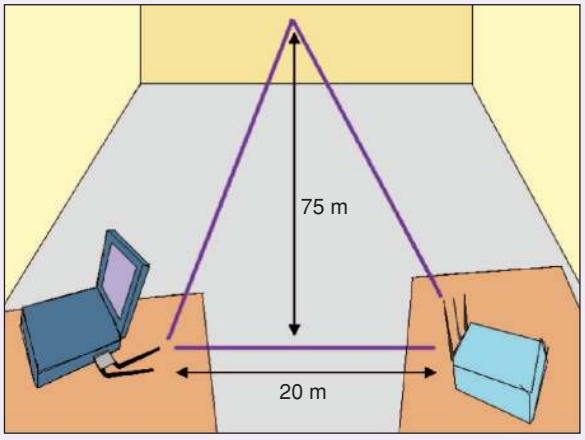

Figure 6. Example of large delay spread.

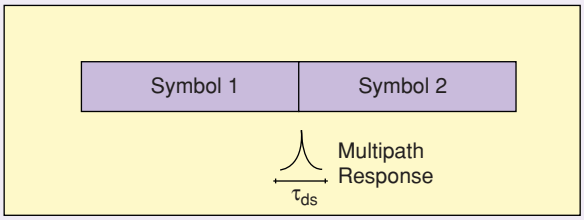

Figure 7. Example of flat fading: use of large symbol time.

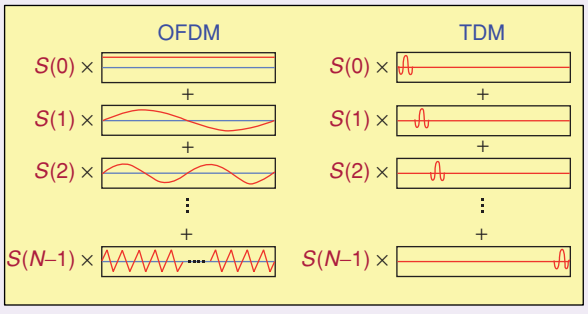

Figure 8. Use of OFDM versus Time-Division Multiplexing (TDM).

From [11], the coherence bandwidth, B_C, may be defined as either $B_C = (1/5\,\sigma_\tau)$, or $B_C = (1/50\,\sigma_\tau)$, where σ_τ is the RMS delay spread, depending on whether the frequencies within the bandwidth should have a correlation function above 0.5 or 0.9, respectively.

Based on the delay spread, flat fading concepts above, we now consider the use of OFDM. With OFDM, the channel can be viewed as N narrowband channels. The transmitter, using OFDM modulation, can be written as:

$$s(t) = \sum_{k=0}^{N-1} S(k) e^{j2\pi kt/T_S} \tag{14}$$

From the above equation, we see that N data symbols, $S(0)$ to $S(N-1)$, are sent on N different tones (indexed by k) over the entire symbol time T_s. This allows for a larger symbol time compared with sending N symbols in time, each with symbol time T_s/N, for the same data throughput (see Figure 8). Thus, using OFDM allows for an efficient use of channel bandwidth as well as providing a large symbol time for handling frequency-selective fading.

For 802.11n in 20 MHz mode, the OFDM transmitter uses a 64-point FFT, and symbol time $T_s = 3.2$ us (same as 11a/g). Thus, flat-fading should occur when the rms delay spread is less than 3.2 us/10, or 320 ns.

OFDM modulation also includes a 16-sample (or 800 ns) cyclic prefix. The cyclic prefix, or CP, is a set of samples added to the front of the OFDM symbol which creates a periodic extension of the frequencies within the symbol. The addition of CP symbol allows the linear convolution of the transmitted OFDM symbol with the channel to appear as circular convolution [13], [15]. Thus, the effect of the channel can be viewed as multiplication in the frequency domain. The addition of an 800 ns cyclic prefix also allows the receiver to handle a channel delay spread of around 600 ns (assuming 200 ns is reserved for any symbol timing estimation inaccuracy) before the circular convolution assumption becomes invalid.

Thus, using OFDM with cyclic prefix, (see Figure 9) the received symbol for a SISO channel can be written as (in frequency domain):

$$R(k) = H(k)S(k) + N(k) \tag{15}$$

where the channel response H(k) for each sub-carrier is a complex, scalar value.

Thus, the MIMO channel can be written as (in frequency-domain, for each sub-carrier k):

$$H(k) = \begin{bmatrix} h_{1,1}(k) & \cdots & h_{1,M}(k) \\ \vdots & \ddots & \vdots \\ h_{N,1}(k) & \cdots & h_{N,M}(k) \end{bmatrix} \quad (16)$$

where each element, $h_{i,j}$, of $H(k)$ is a complex scalar element representing the channel gain and phase for subcarrier k.

III.1.3 MIMO Channel Modeling: TGn Channel Models

Here, we outline the approach for MIMO channel modeling described in the TGn channel model specification [7]. This document describes a set of indoor MIMO channel models (referred to as the TGn channel models), developed and based on numerous experimental results reported in literature. The TGn channel models consist of six models (A to F), which represent a variety of indoor environments, ranging from small environments (A to C), such as residential homes, with rms delay spreads from 0 to 30 ns, up to larger areas (D to F), such as open spaces and office environments, with rms delay spreads from 50 to 150 ns.

Briefly, the channel modeling process used involves treating reflection paths as clusters of rays. Each cluster has a power delay profile (power at different delays, i.e., taps in discrete time), which is used in finding MIMO channel tap coefficients. This approach, developed by Saleh and Valenzuela [16], is known as cluster modeling (discussed in the next sub-section). An illustration of a single cluster is shown in Figure 10.

The parameters used to model each cluster are the angle-of-departure (AoD) from the transmitter, the angle-of-arrival (AoA) at the receiver, and the angular spread (AS) at both stations (one AS value for each). These values are based on the environment configuration as well as the orientation of the two WLAN devices, as can be seen in Figure 10. Note that the cluster powers and AS values are used to find the power angular spectrum (PAS) (i.e., the power distribution over angle) at both stations. The angular spread (AS) is the second moment (i.e., variance) of the PAS.

From the above parameters, the AoD and transmit-side PAS are used to determine the correlation between the transmit antenna signals (transmit correlation matrix R_{tx}). Also, the AoA and receive-side PAS are used to find the correlation between receive antenna signals (receive correlation matrix R_{rx}). The R_{tx} and R_{rx} correlation matrices are then used to determine the channel tap matrices. The above-described correlation across transmit and receive antennas result in spatially-dependent fading, often referred to as spatial selectivity [14].

The cluster modeling approach, followed by the MIMO channel model, and the process for finding channel matrices based on the above mentioned parameters, is described in the following subsections.

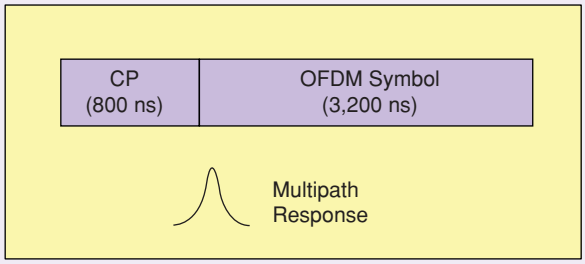

Figure 9. Use of OFDM with cyclic prefix.

III.1.3.1 Cluster Modeling

This subsection outlines the cluster modeling approach by Saleh and Valenzuela [16], discussed in [7], and described in many references including [1], [11], and [17]. The purpose of this sub-section is to illustrate how cluster modeling represents the scattering that occurs with reflection paths as well as the resulting signal fading.

In general, the wireless channel is considered to consist of multipath components (or MPCs), caused by reflecting objects which are randomly located within an environment. The random arrival times (or excess delays) of the MPCs, in this case, would be modeled using a Poisson distribution. However, experiments have indicated that the MPCs generally arrive in groups, or clusters [1], [16], [17].

Based on the above, the approach by Saleh and Valenzuela models the MPCs using clusters, where the arrivals of MPCs within a cluster (referred to as rays) are modeled with a Poisson distribution with a certain average inter-arrival time (i.e., arrival rate). Additionally, the arrivals of the clusters themselves (i.e., groups of rays) are also modeled with a Poisson distribution using a different (larger) average inter-arrival rate.

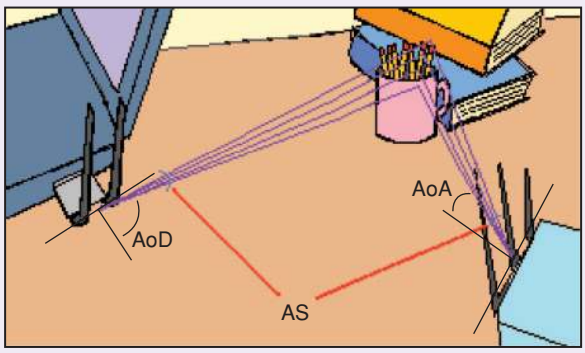

Figure 10. Example of modeling for one cluster.

In general, the channel impulse response with this model is [16], [17]:

$$h(t) = \sum_{l=0}^{\infty} \sum_{k=0}^{\infty} \left(\beta_{k,l} e^{j\varphi_{k,l}} \partial(t - T_l - \tau_{k,l}) \right) \qquad (17)$$

where:

- l and k are the indices for the cluster, and ray within a cluster, respectively,
- $\beta_{k,l}$ is the amplitude for the k-th ray within the l-th cluster,
- $\phi_{k,l}$ is the phase for the k-th ray within the l-th cluster,
- T_l is the arrival time of the first ray of the l-th cluster,
- $\tau_{k,l}$ is the delay of the k-th ray within the l-th cluster.

The cluster and ray arrival times (T_l and $\tau_{k,l}$) are modeled with Poisson distributions:

$$\begin{aligned} pdf(T_l|T_{l-1}) &= \Lambda \exp(-\Lambda(T_l - T_{l-1})) \qquad T_l > T_{l-1} \\ pdf(\tau_{k,l}|\tau_{k-1,l}) &= \lambda \exp(-\lambda(\tau_{k,l} - \tau_{k-1,l})) \qquad \tau_{k,l} > \tau_{k-1,l} \end{aligned} \qquad (18)$$

where Λ is the average arrival rate of the clusters, and λ is the average arrival rate of the rays within a cluster. Example values for these arrival rates are around 200 ns for $1/\Lambda$, and between 5–10 ns for $1/\lambda$, based on the measurement data from [16].

In addition, the powers of the rays within a cluster as well as the powers of the clusters themselves, were found to exponentially decrease with delay, (at different decay rates), modeled as [7], [16], [17]:

$$\begin{aligned} E\left[\beta_{k,l}^2\right] &= E[\beta^2(T_l, \tau_{k,l})] \\ &= E[\beta^2(0,0)] \exp(-T_l/\Gamma) \exp(-\tau_{k,l}/\gamma) \end{aligned} \qquad (19)$$

where Γ is the inter-cluster decay rate, γ is the intra-cluster decay rate, and $E[\beta^2(0,0)]$ is the average power of the first arrival (ray) of the first cluster.

Equation (19) shows that the average ray power $\beta_{k,l}^2$ is related to the power of the first ray arrival by a double exponential decay law [7] with a different decay rate for the decay between clusters, and the decay between rays within a cluster. This model for channel power versus delay is referred to as the power delay profile (PDP). The resulting PDP when considering only the last exponential term in (19) (i.e., just the rays within a single cluster) is referred to as the PDP of the cluster (or cluster PDP) in this section.

In addition, the ray arrival phases $\phi_{k,l}$ in (17) are considered uniformly distributed, and the arrival amplitudes $\beta_{k,l}$ Rayleigh distributed [16], [17]:

$$pdf(r) = \frac{r}{\sigma^2} \exp\left(\frac{-r^2}{2\sigma^2}\right) \qquad (20)$$

where r is the amplitude, $\beta_{k,l}$, and $2\sigma^2$ is the mean-square value of r, $E[r^2]$, which is equivalent to $E[\beta_{k,l}^2]$ from (19).

Note that the Rayleigh amplitude and uniform phase distributions were suggested by Saleh and Valenzuela [16], since a 5 ns time resolution was used for the signal measurements. These distributions result in $\beta_{k,l}e^{j\varphi_{k,l}}$ following a complex Gaussian process, which describes what would be expected if each "ray" was a summation of numerous independent rays arriving within each 5 ns time interval However, it is noted in [16] that other models (for example, a log-normal distribution) may better fit the measurement data.

The above cluster model is considered to have the following intuition: The rays forming a cluster are generally considered to represent the multiple objects/ reflections that may exist in the regions surrounding the receiver, transmitter, or the main reflecting path, an example of which is illustrated in Figure 10 (note that sufficiently random scattering solely around the transmitter or receiver would result in an even distribution of power across angle, i.e., no change in the dominant AoD or AoA, respectively, compared to the direct line-of-sight case).

Each reflection results in attenuation, depending on the reflecting material (affecting the Γ, γ decay rates) as well as the propagation delay increase. Additionally, based on the configuration of the environment, the cluster and ray arrival times, T_l and $\tau_{k,l}$, can be determined. However, for simulation modeling, these parameters are considered to follow Poisson distributions (i.e., for modeling a random environment configuration).

Note that the TGn channel model specification [7] provides pre-computed cluster PDP tables for each channel model, and that the above description of cluster modeling, forming PDPs, was intended to illustrate the approach used in modeling the reflection paths. Also, in some cases, the clusters overlap (based on inter-arrival times), in which case the cluster PDPs are combined to obtain the overall channel PDP (described in Subsection III.1.3.3).

The general form of the MIMO channel model, as well as the approach for finding the channel tap coefficients (based on cluster PDPs, other parameters) is described below.

III.1.3.2 MIMO Channel Model

Based on the approach in [18] and [19] as well as the description in the previous sub-section, the discrete-time version of the MIMO channel can be written as:

$$H_{Total}(t) = \sum_{l=0}^{L-1} H_l \delta(t - \tau_l) \tag{21}$$

and the output of the MIMO channel as:

$$y(t) = \sum_{l=0}^{L-1} H_l x(t - \tau_l) \qquad \text{or}$$

$$y(t) = \sum_{l=0}^{L-1} H_{Total}(\tau_l) x(t - \tau_l) \tag{22}$$

where:

- $x(t)$ is the input vector of all Tx antennas at time t,
- $y(t)$ is the output vector of all Rx antennas at time t,
- $\delta(t)$ is the delta function, and
- H_l is a MIMO channel coefficient (or channel tap matrix) with tap index l and delay τ_l (i.e., sampled at time τ_l).

Note the MIMO channel can be seen as a linear convolution of the channel response H_{Total} and input vector $x(t)$, where H_{Total} is a sequence of matrices, and $x(t)$ is a sequence of vectors, similar to (5), (6), except (21), (22) are discrete-time representations. The delay values τ_l for the channel taps are specified in [7] for each channel model.

III.1.3.3 Channel Tap Matrices

In general, the wireless MIMO channel consists of a line-of-sight (LOS) component as well as non light-of-sight (NLOS) components. For the TGn channel models [7], each channel tap, matrix H_l, is written as the sum of a constant, LOS matrix and a variable, NLOS, Rayleigh matrix.

Note that the LOS matrix is considered constant in [7], under the assumption that the transmitter and receiver locations are fixed, and only the surrounding objects are in motion, affecting the NLOS matrix. This assumption simplifies the computation of most modeling parameters, (the LOS matrix, PAS, and R_{tx}, R_{rx} correlation matrices, described later), and also reflects the typical usage scenario for WLAN devices.

For a 4Tx-4Rx antenna configuration, the channel matrices H_l can be written as follows:

$$H_l = \sqrt{P_l}\left(\sqrt{\frac{K}{K+1}}\begin{bmatrix} e^{j\phi_{11}} & e^{j\phi_{12}} & e^{j\phi_{13}} & e^{j\phi_{14}} \\ e^{j\phi_{21}} & e^{j\phi_{22}} & e^{j\phi_{23}} & e^{j\phi_{24}} \\ e^{j\phi_{31}} & e^{j\phi_{32}} & e^{j\phi_{33}} & e^{j\phi_{34}} \\ e^{j\phi_{41}} & e^{j\phi_{42}} & e^{j\phi_{43}} & e^{j\phi_{44}} \end{bmatrix} + \sqrt{\frac{1}{K+1}}\begin{bmatrix} X_{11} & X_{12} & X_{13} & X_{14} \\ X_{21} & X_{22} & X_{23} & X_{24} \\ X_{31} & X_{32} & X_{33} & X_{34} \\ X_{41} & X_{42} & X_{43} & X_{44} \end{bmatrix}\right) \tag{23}$$

where:

- P_l is the overall power of channel tap l,
- K is the Ricean K-factor (described later in this subsection),
- $e^{j\phi_{ij}}$ are the elements for the fixed LOS matrix, and
- X_{ij} are correlated (between i-th receive, j-th transmit antenna) zero-mean, unit variance, complex Gaussian random variable coefficients for the NLOS, Rayleigh matrix.

Note that the above complex Gaussian assumption for X_{ij} is valid assuming each tap is formed by several individual rays (based on cluster modeling). The overall tap power P_l represents the sum of the fixed LOS and variable NLOS powers. The set of values P_l are often referred to as the power delay profile, or PDP.

For each channel model in [7], instead of specifying the values of P_l directly, the power delay profile of each cluster (i.e., cluster tap powers) is specified, which is used to compute P_l (i.e., the sum of all overlapping cluster tap powers at the same delay as well as the LOS component, if applicable). This approach is used since the cluster tap powers are also required for computing the power angular spectrum (described later).

The parameter, K, in equation (23) (known as the Ricean K-factor) represents the relative strength of the LOS component. When $K = 0$, equation (23) can easily be seen to represent an NLOS channel (the LOS matrix term is removed). In this case, the values of H_l follow a Rayleigh distribution. Otherwise, (23) describes a LOS channel (consists of a LOS component, which may or may not contain NLOS components), which follows a Ricean distribution. The Rayleigh and Ricean distributions are described in detail in [11].

Note that as K increases, the channel becomes increasingly correlated in space (based on the LOS matrix shown later), which reduces the potential for multiplexing gain for the MIMO system [14]. This is described in more detail later, when MIMO techniques are covered. For the Ricean K-factor, typical values for the LOS channel models described in [7] range from 0 dB to 6 dB. For NLOS channels, $K = -\infty$ (in dB) is used.

The fixed LOS matrix (elements, $e^{j\phi_{ij}}$) can be written as [20]:

$$\begin{bmatrix} e^{j\phi_{11}} & e^{j\phi_{12}} & e^{j\phi_{13}} & e^{j\phi_{14}} \\ e^{j\phi_{21}} & e^{j\phi_{22}} & e^{j\phi_{23}} & e^{j\phi_{24}} \\ e^{j\phi_{31}} & e^{j\phi_{32}} & e^{j\phi_{33}} & e^{j\phi_{34}} \\ e^{j\phi_{41}} & e^{j\phi_{42}} & e^{j\phi_{43}} & e^{j\phi_{44}} \end{bmatrix} = \exp\left(j2\pi \frac{v_O}{\lambda} t \cos(\pi/4)\right) \cdot S \tag{24}$$

where S is the Rice steering matrix:

$$S = \begin{bmatrix} 1 \\ \exp\left(j2\pi \frac{d_{Rx}}{\lambda} \sin(AoA_{Rx})\right) \\ \cdots \\ \exp\left(j2\pi \frac{d_{Rx}}{\lambda} \sin[(n_{Rx}-1)AoA_{Rx}]\right) \end{bmatrix} \times \begin{bmatrix} 1 \\ \exp\left(j2\pi \frac{d_{Tx}}{\lambda} \sin(AoD_{Tx})\right) \\ \cdots \\ \exp\left(j2\pi \frac{d_{Tx}}{\lambda} \sin[(n_{Tx}-1)AoD_{Tx}]\right) \end{bmatrix}^T \quad (25)$$

where:

- λ is the wavelength (shown previously),
- n_{Tx}, n_{Rx} are the number of transmit, receive antennas,
- AoD_{Tx}, AoA_{Rx} are the angle of departure (from the transmit antennas) and angle of arrival (at the receive antennas),
- d_{Tx}, d_{Rx} are the spacing between the transmit, receive antennas (typical spacing used is $d = \lambda/2$ between antennas).

Note that, for all channel models in [7], the LOS contribution is only applied to the first tap (i.e., delay 0), as the LOS path clearly arrives first, and experiences no reflections (i.e., not spread across time). The LOS component is added on top of the NLOS clusters, resulting in a higher overall power than the original NLOS power delay profiles (i.e., the first tap power should not be scaled down to match the original NLOS PDPs).

For combining cluster tap powers to compute the overall tap powers, consider that, from [11], the total received power for an antenna, P_r, is expressed as:

$$P_r = \int_0^{2\pi} AG(\alpha)p(\alpha)d\alpha \quad (26)$$

where:

- A is the average antenna received power,
- $G(\alpha)$ is the antenna gain for angle of arrival α,
- $p(\alpha)d\alpha$ is the fraction of power arriving within $d\alpha$ of angle α.

From equation (26), we see that if the mean AoA's of two clusters are separated by more than their individual AS's (angular spreads), the powers should be summed. However, if the power of two clusters arrive with the same angle α the phase difference between them should also be considered, to determine if they will combine constructively or destructively. But since, with the power delay profiles in [7], the cluster powers are given at the same tap delay (i.e., arrive at the same time), the phase difference is minimal, and the powers may be summed in this case as well.

Based on the above, we see that all cluster tap powers with the same delay may always be summed to determine the overall power at the receiving antenna for that delay.

III.1.3.4 Antenna Correlation Modeling

For correlating the elements, X_{ij}, of the NLOS, Rayleigh matrix (matrix X below), we can use:

$$X = \sqrt{R_{rx}} \cdot H_{iid} \cdot \sqrt{R_{tx}}^T \quad (27)$$

where:

- R_{tx}, R_{rx} are transmit and receive correlation matrices, and
- H_{iid} is a matrix of independent, unit variance, zero-mean, complex random variables (standard Rayleigh fading MIMO channel matrix).

Alternatively, an approach using the Kronecker product may be used:

$$X = \sqrt{R_{tx} \otimes R_{rx}} \cdot H_{iid} \quad (28)$$

where, for the above approach, H_{iid} is an array instead of a matrix.

The R_{tx}, R_{rx} correlation matrices, for a 4x4 MIMO channel, can be written as:

$$R_{tx} = \begin{bmatrix} 1 & \rho_{tx12} & \rho_{tx13} & \rho_{tx14} \\ \rho_{tx21} & 1 & \rho_{tx23} & \rho_{tx24} \\ \rho_{tx31} & \rho_{tx32} & 1 & \rho_{tx34} \\ \rho_{tx41} & \rho_{tx42} & \rho_{tx43} & 1 \end{bmatrix},$$
$$R_{rx} = \begin{bmatrix} 1 & \rho_{rx12} & \rho_{rx13} & \rho_{rx14} \\ \rho_{rx21} & 1 & \rho_{rx23} & \rho_{rx24} \\ \rho_{rx31} & \rho_{rx32} & 1 & \rho_{rx34} \\ \rho_{rx41} & \rho_{rx42} & \rho_{rx43} & 1 \end{bmatrix} \quad (29)$$

where:

- ρ_{txij} are the complex correlation coefficients between the i-th and j-th transmit antennas, and
- ρ_{rxij} are the complex correlation coefficients between the i-th and j-th receive antennas.

Computing the above complex correlation coefficients for each tap requires the power angular spectrum (PAS) and its second moment—angular spread (AS), the mean AoA and AoD values, and the power of each cluster tap.

In addition, the antenna configuration needs to be considered. The typical configuration used is the uniform linear array (ULA) configuration (i.e., a line of evenly-spaced antennas). With this configuration, each complex correlation coefficient can be written as:

$$\rho = R_{XX}(D) + jR_{XY}(D) \quad (30)$$

where:

- R_{XX} is the cross-correlation between the real parts (same as the cross-correlation of the imaginary

parts) of the i-th and j-th transmit(or receive) antennas,

- R_{XY} is the cross-correlation between the real and imaginary parts of the i-th and j-th transmit (or receive) antennas, and
- $D = 2\pi d/\lambda$, where d is the antenna element spacing, $\lambda = c/f_c$ is the wavelength, f_c is the carrier frequency, and c is the speed of light.

The cross-correlations, $R_{XX}(D)$ and $R_{XY}(D)$, are defined as:

$$R_{XX}(D) = \int_{-\pi}^{\pi} \cos(D \sin\phi)\, PAS(\phi) d\phi$$
$$R_{XY}(D) = \int_{-\pi}^{\pi} \sin(D \sin\phi)\, PAS(\phi) d\phi \qquad (31)$$

The PAS (power angular spectrum) in (31) defines the distribution of signal power over angle. The three main PAS shapes are uniform, truncated Gaussian, and truncated Laplacian. Examples of each are illustrated in Figure 11.

Of the three PAS shapes shown, the channel models in [7] use the truncated Laplacian PAS shape, which was found to match closely the angle of arrival statistics within a cluster for urban environments [18]. The uniform PAS shape typically models canyon-type environments (where the angle of arrival is considered to be evenly distributed), while the truncated Gaussian PAS shape is used to model environments where each cluster is considered to consist of numerous, randomly-placed scattering objects, giving rise to a Gaussian-distributed angle of arrival.

The truncated Laplacian PAS can be written as [18]:

$$PAS(\phi) = \sum_{k=1}^{N_c} \frac{Q_k}{\sigma_k\sqrt{2}} \exp\left(\frac{-\sqrt{2}|\phi - \phi_{o,k}|}{\sigma_k}\right)\{u(\phi - (\phi_{0,k} - \Delta\phi_k)) - u(\phi - (\phi_{0,k} + \Delta\phi_k))\} \qquad (32)$$

where:

- $u(n)$ is the step function,
- N_c is the number of clusters,
- $\phi_{0,k}$ is the mean AoA (or AoD) for cluster k,
- $\Delta\phi_k$ defines the range of the truncated Laplacian for cluster k,
- σ_k is the standard deviation of the PAS (i.e., angular spread, or AS, value) for each cluster (AS values are given in [7]), and
- Q_k are normalization constants, based on the cluster powers (also given in [7]), which satisfy:

$$\sum_{k=1}^{N_c} Q_k \left[1 - \exp\left(\frac{-\sqrt{2}\Delta\phi_k}{\sigma_k}\right)\right] = 1 \qquad (33)$$

The equations for $R_{XX}(D)$ and $R_{XY}(D)$ shown in (31) are computed for each tap, considering the power, AS, and mean AoA (or AoD) values for all clusters at that tap delay. Also, the expressions are evaluated separately for transmit and receive correlation coefficients (the coefficients ρ_{txij} are computed using the mean AoD and AS across the transmit antennas, and ρ_{rxij} using the mean AoA and AS across the receive antennas).

Moreover, because the above channel model parameters are fixed values (provided in [7]), the ρ_{txij} and ρ_{rxij} correlation coefficients (and thus the R_{tx} and R_{rx} correlation matrices) for each channel tap need to be computed only once for any of the channel models.

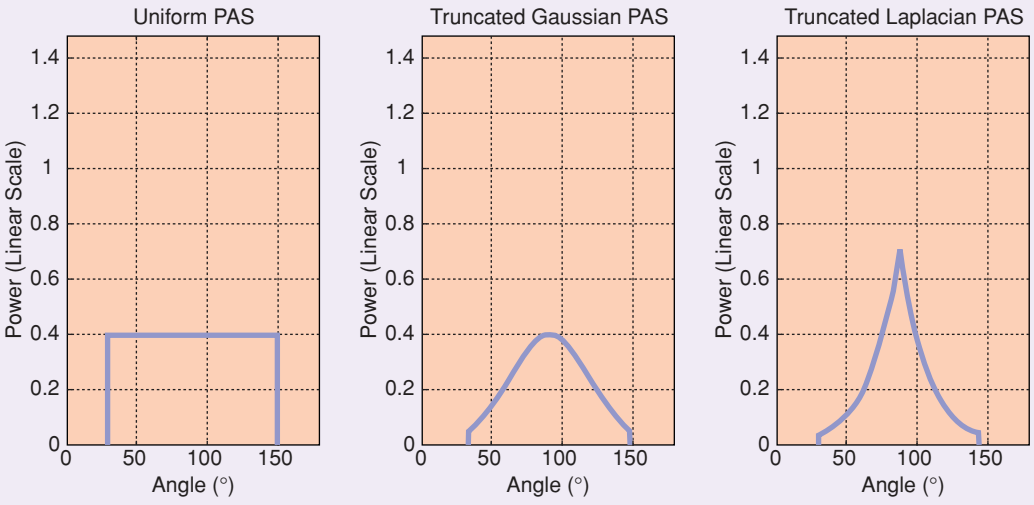

Figure 11. Uniform, truncated Gaussian, and truncated Laplacian PAS shapes.

Note the fact that these channel parameters are fixed corresponds to selecting a specific transmitter-receiver-environment configuration (i.e., all angles specified) which remains stationary throughout the channel model simulation.

III.1.3.5 Modeling Doppler Components

For indoor wireless channels, the typical fading effect scenario involves human-based motion (i.e. people walking between stationary transmitter, receiver systems). These fading effects can be described by the following Doppler power spectrum:

$$S(f) = \frac{1}{1 + A\left(\frac{f}{f_d}\right)^2} \tag{34}$$

where:

- A is a constant, defined to set $S(f) = 0.1$ (a 10 dB drop) at frequency f_d (thus: $A = 9$), and
- f_d is the Doppler spread, defined as: $f_d = v_o/\lambda$, with v_o representing the environmental speed (around 1.2 km/h proposed) and where $\lambda = c/f_c$ is the wavelength (shown previously).

The corresponding autocorrelation function (i.e., inverse Fourier transform of $S(f)$), is:

$$R = \frac{\pi f_d}{\sqrt{A}} \exp\left(-\frac{2\pi f_d \Delta t}{\sqrt{A}}\right) \tag{35}$$

The Doppler spectral shape determines the time-domain fading as well as the temporal correlation and fading slope behavior, and is used in Rayleigh fading simulators to produce fading waveforms with the proper time correlation [11].

Since the $S(f)$ function describes the power spectrum of the Doppler fading, it can be used as a spectral filter to shape the Gaussian random signals in the frequency domain, which should result, after an IFFT, in accurate time-domain waveforms of Doppler fading [11]. Note that the number of points (or taps) should be selected to give sufficient frequency resolution to show the spectrum around the Doppler spread, f_d (note that f_d is around 3 Hz at 2.4 GHz, and around 6 Hz at 5.2 GHz).

Thus, the elements of H_{iid} (independent, zero-mean, unit variance, complex Gaussian random variables) may be individually filtered using the above technique so that the Rayleigh matrix produces the desired Doppler fading.

In addition, another Doppler component, resulting from fluorescent lights, has been shown to result in a channel where signal reflections are added and removed at twice the power line frequency, resulting in frequency selective amplitude modulation [7]. This effect is included in channel models D and E only, which are intended to model office environments (D – typical office, E – large office).

The effect is modeled by modulating several of the channel taps in order to simulate the desired amplitude modulation. The modulator used is randomized to create AM distortions, period shapes, resembling the measured data.

The modulating function, from [7], is:

$$g(t) = \sum_{l=0}^{2} A_l \exp\{j(4\pi(2l+1)f_m t + \varphi_l)\} \tag{36}$$

where:

- A_l are relative harmonic amplitudes ($A_0 = 0$ dB, $A_1 = -15$ dB, $A_2 = -20$ dB),
- f_m is the power line frequency (U.S.: 60 Hz, Europe: 50 Hz),
- φ_t is a series of i.i.d. phase RV's, uniformly distributed: $U[0, 2\pi)$.

From (36), we see that three tones are used for the modulating signal: the fundamental and 2 odd harmonics (100 Hz, 300 Hz, and 500 Hz for Europe).

The modulating signal in (33) is applied to three of the channel taps using:

$$c'(t) = c(t)(1 + \alpha \cdot g(t)) \tag{37}$$

where:

- $c(t)$ and $c'(t)$ are the old, new tap values, respectively,
- α is the normalization constant.

The normalization constant, α, is selected to ensure that the total modulation energy satisfies the ratio provided by random variable, X, given in (38), which models the desired I/C, or interference to carrier energy ratio (where interference is the modulation energy in the modulated taps, and carrier energy is the energy of the channel response):

$$\frac{I}{C} = X^2, \tag{38}$$

where X is a Gaussian random variable with mean $\mu = 0.0203$, and variance $\sigma^2 = 0.0107^2$.

III.2 MIMO Signal Processing Techniques

With the indoor wireless channel under MIMO now described, this section presents the main signal processing techniques used in realizing the benefits of multiple antennas. The techniques described are spatial-division multiplexing (SDM), MIMO channel estimation and detection, space-time block coding (STBC), and transmitter beamforming. Note that channel estimation techniques are discussed last in order to better show how the approach used for channel estimation may influence the other signal processing techniques.

III.2.1 Spatial-Division Multiplexing (SDM)

To achieve higher throughputs using multiple antennas, the key technique used is spatial-division multiplexing (SDM). As the name implies, this technique involves the multiplexing of multiple data streams across spatial dimensions (i.e., transmit antennas separated by location, or space). With SDM, multiple transmit antennas, appropriately spaced, are used to transmit independent data streams, which can individually be recovered at the receiver. Figure 12 illustrates the transmitter architecture using SDM.

Regarding the antenna spacing, note that, from the channel modeling description given previously, a shift in distance on the order of the wavelength, λ, dramatically affects fading (since shifting by λ results in a 2π carrier phase change). A common choice for antenna spacing is $\lambda/2$ ($= 2.7$ cm with 5.2 GHz carrier), for both transmit and receive antennas.

It is important to consider, however, that the benefit of using SDM depends on the MIMO channel. As described previously, the MIMO channel can be modeled in matrix form, for each sub-carrier, as

$$[R(k) = H(k)S(k) + N(k)]$$

with

$$H(k) = \begin{bmatrix} h_{1,1}(k) & \cdots & h_{1,M}(k) \\ \vdots & \ddots & \vdots \\ h_{N,1}(k) & \cdots & h_{N,M}(k) \end{bmatrix}$$

Based on linear algebra, we readily see that finding a solution for the M-dimensional transmitted vector $S(k)$ requires that the matrix $H(k)$ have a minimum rank of M (i.e., the matrix $H(k)$ should consist of at least M linearly independent row vectors).

Essentially, this means that the channel response seen at each different receive antenna (i.e., the rows of the matrix $H(k)$) should be sufficiently unique so that the transmit vector $S(k)$ can be recovered. Whether this is the case depends on the channel, and is, in general, satisfied in the case where multiple reflection paths exist between the transmitter and receiver (referred to as a rich, or dense multipath, scattering environment [14], [15], [19]), and if the transmit and receive antennas are appropriately spaced to guarantee variation in the signal seen across the receive antennas. We expand on this concept in the MIMO detection, as well as beamforming sub-sections.

III.2.2 MIMO Detection

MIMO detection refers to the process of determining the transmitted data symbols, sent using SDM, from the received signal vector. This requires both separating each transmitted data stream from the other transmitted streams (interference cancellation), as well as performing channel equalization [12]. In this section, we describe the main approaches used to accomplish this: the Zero-Forcing (ZF) and Minimum Mean Squared Error (MMSE) linear detectors, and the Maximum Likelihood (ML) detector.

In discussing MIMO detection, we first consider the basic form for a memoryless MIMO system [12], which can be described by:

$$r = Ha + n \tag{39}$$

where r is the N-dimensional received signal vector, H is the $N \times M$ matrix of channel estimates, a is the M-dimensional transmitted signal, and n is a complex additive white Gaussian noise vector. The transmitted symbol a is chosen from the constellation set S.

Assuming that H is known at the receiver, (i.e., after channel estimation), the various MIMO detectors can be described as follows:

The zero-forcing linear detector selects the linear detector matrix C in order to eliminate interference

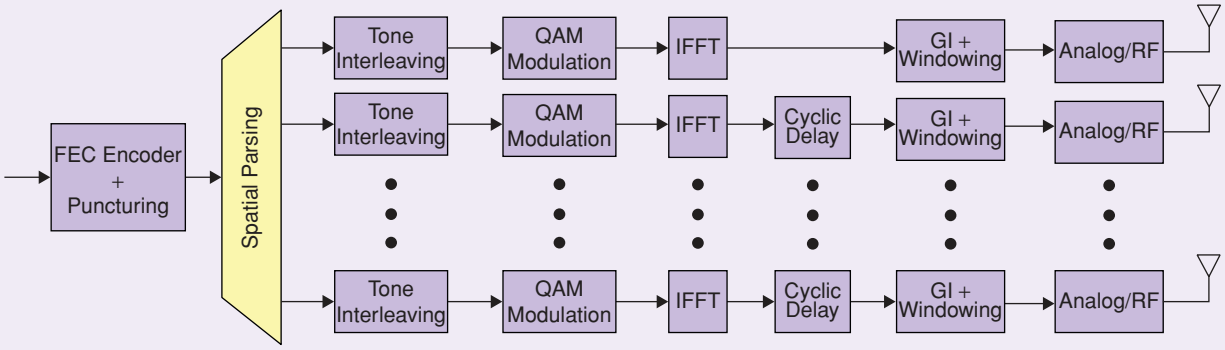

Figure 12. Block diagram of 11n transmitter using SDM.

completely [12]. More precisely, C is chosen such that $CH = I$. This matrix always exists, under the assumption that the columns of H are linearly independent. If the channel has the same number of inputs as outputs, H is a square matrix and the ZF linear detector has a unique solution: $C{=}H^{-1}$. For a channel with more outputs than inputs, $N > M$, the number of solutions for $CH = I$ is infinite. In this case, the ZF linear detector is the unique solution that minimizes MSE $= E[\|Cr - a\|^2]$.

The ZF linear detector has the form: $C{=}(H^H H)^{-1}H^H$, also known as the Moore-Penrose pseudoinverse of H. If H is invertible, the matrix C is just H^{-1}.

A drawback of the ZF linear detector is that it focuses solely on interference cancellation. In this process, it can also remove signal energy that projects onto the interference subspace, even when the interference is significantly lower than the desired signal. A better approach would be to choose matrix C considering both signal energy loss as well as interference cancellation, since maximizing desired signal energy at the expense of suboptimal interference cancellation is more ideal.

The MMSE linear detector chooses C to minimize MSE $= E[\|Cr - a\|^2]$ without the additional constraint $CH = I$. The MMSE detector can equivalently be written to minimize MSE $= tr\{R_e\}$, where $R_e = E[(Cr - a)(Cr - a)^H]$.

Expanding R_e yields:

$$\begin{aligned} R_e &= E[(Cr - a)(Cr - a)^H] \\ &= CR_rC^H + I - H^HC^H - CH \\ &= \left(C - H^HR_r^{-1}\right)R_r\left(C - H^HR_r^{-1}\right)^H \\ &\quad + N_o(H^HH + N_oI)^{-1} \end{aligned}$$

where $R_r = E[rr^H]$ (received autocorrelation matrix) and $E[aa^H] = I$ (since a is zero-mean, Gaussian). Note only the first term depends on C, and is minimized when $C = H^HR_r^{-1}$. Thus, we can write C as either: $C = H^H(HH^H + N_oI)^{-1}$ or $C = (H^HH + N_oI)^{-1}H^H$.

For the ML detector, an exhaustive search across all valid sequences for the transmitted symbol (denoted as s), is performed. This operation can be written as [12]:

$$s = \arg\min_{s\in S}\|r - Hs\|^2 \tag{40}$$

The ML detector provides improved performance over ZF, MMSE linear detectors described previously. From the above equation, we observe that when the correct symbol is found, the mean-square error is: MSE $= N_0$, which is clearly ideal.

However, the complexity order of performing an exhaustive search for ML detection makes the approach unattractive for practical applications. The algorithm runs in exponential time (searches through B^M points) compared to the ZF and MMSE linear detectors, which run in polynomial time, since both require only one matrix multiplication (NM multiplies to perform: $y = Cr$) per data frame. Note that both linear detectors require two matrix multiplies and one matrix inversion initially to form the detector matrix C.

III.2.3 Space-Time Block Coding

Space-time block codes (STBC) are used to achieve spatial diversity using multiple transmit antennas [13]. STBC codes offer advantages versus the other main coding scheme, space-time trellis codes (STTC), in that it can achieve full diversity gain with low complexity, whereas STTC codes increase in decoding complexity as the constellation size, state number, code length increases [14]. The most common form of STBC coding, known as Alamouti coding, is the foundation for the space-time coding used in the IEEE 802.11n draft, and is described below.

The basic Alamouti code encodes one spatial stream into two space-time streams as follows:

For inputs x_1 and x_2 (in time), the outputs are, from [8]:

$$y_1 = \begin{bmatrix} x_1 \\ -x_2^* \end{bmatrix} \qquad y_2 = \begin{bmatrix} x_2 \\ x_1^* \end{bmatrix} \tag{41}$$

Using this space-time code, the first spatial stream transmits symbols: x_1 and x_2 (in time), and the second transmits: $-x_2^*$ and x_1^*. Note that with this form for the STBC, the first spatial stream transmits the original sequence unaltered, while the second stream provides space-time coding.

At the receiver, the received symbols are:

$$\begin{aligned} r_1 &= [\,h_1 \quad h_2\,] \cdot \begin{bmatrix} x_1 \\ -x_2^* \end{bmatrix} + n_1 \\ r_2 &= [\,h_1 \quad h_2\,] \cdot \begin{bmatrix} x_2 \\ x_1^* \end{bmatrix} + n_2 \end{aligned} \tag{42}$$

In the receiver, we can recover the transmitted data from the received data by forming the vector $\{r_1, r_2^*\}$ using one receive antenna (note that we are using transmit diversity here, with only one receive antenna, or a MISO, or multiple-input single-output, channel).

The vector of two received symbols can be expressed (in terms of the transmitted symbols, channel response) as:

$$\begin{bmatrix} r_1 \\ r_2^* \end{bmatrix} = \begin{bmatrix} h_1 & -h_2 \\ h_2^* & h_1^* \end{bmatrix} \cdot \begin{bmatrix} x_1 \\ x_2^* \end{bmatrix} + \begin{bmatrix} n_1 \\ n_2^* \end{bmatrix} \tag{43}$$

From the above, we see that, assuming that the noise samples n_1, n_2, are independent samples taken from a zero-mean, white Gaussian process, the noise will remain white, i.e., $\mathrm{E}[nn^*] = N_o I$. Also, since the two columns of the channel matrix in (43) (call this matrix H_{eff}) are orthogonal, a suitable matched filter (MMF) is H_{eff}^H.

After applying this matched filter:

$$\begin{bmatrix} y_1 \\ y_2^* \end{bmatrix} = H_{eff}^H H_{eff} \begin{bmatrix} x_1 \\ x_2^* \end{bmatrix} + H_{eff}^H \begin{bmatrix} n_1 \\ n_2^* \end{bmatrix} = \|H\|^2 \begin{bmatrix} x_1 \\ x_2^* \end{bmatrix} + H_{eff}^H \begin{bmatrix} n_1 \\ n_2^* \end{bmatrix} \tag{44}$$

where $H^H H$ can be seen to be $|H|^2$I, with $|H|^2 = |h_1|^2 + |h_2|^2$. Note that the channel response is diagonalized (since the columns of H_{eff} are orthogonal). So, after applying the matched filter, there is no interference of x_1 with x_2^*, and vice versa. Moreover, the noise also remains white after equalization, since:

$$\begin{aligned} E[\vec{n}\vec{n}^H] &= E\left[H_{eff}^H n n^H H_{eff}\right] \\ &= H_{eff}^H E[nn^H] H_{eff} \\ &= H_{eff}^H \cdot N_o I \cdot H_{eff} \\ &= N_o \|H\|^2 I \end{aligned} \tag{45}$$

Thus, the ML detection for x_1, x_2 is greatly simplified, since applying a simple slicer to each symbol (after conjugation of x_2^*) may be used to obtain the ML solution (since there is no interference between x_1 and x_2^*, and the noise is white).

For the 802.11n proposals, various combinations of STBC and spatial-division multiplexing (SDM) may be optionally applied. Next, an example of the STBC coding option mapping two spatial streams to four space-time streams is described.

For the two-spatial stream input vector:

$$x_{2n} = \begin{bmatrix} x_{1,2n} \\ x_{2,2n} \end{bmatrix} \qquad x_{2n+1} = \begin{bmatrix} x_{1,2n+1} \\ x_{2,2n+1} \end{bmatrix} \tag{46}$$

the space-time coding output is:

$$y_1 = \begin{bmatrix} x_{1,2n} \\ -x_{1,2n+1}^* \\ x_{2,2n} \\ -x_{2,2n+1}^* \end{bmatrix} \qquad y_2 = \begin{bmatrix} x_{1,2n+1} \\ x_{1,2n}^* \\ x_{2,2n+1} \\ x_{2,2n}^* \end{bmatrix} \tag{47}$$

Note that the first two output spatial streams are the space-time coding of the first input spatial stream, while the other two output spatial streams are the space-time coding of the second input spatial stream. Thus, the two input spatial streams are space-time coded to four output spatial streams. Note that, at the receiver, only two antennas are used, making the system a 4x2 MIMO system.

The received symbols are (for Rx antenna 1):

$$\begin{aligned} r_{1,2n} &= [\, h_{1,1} \quad h_{1,2} \quad h_{1,3} \quad h_{1,4} \,] \cdot \begin{bmatrix} x_{1,2n} \\ -x_{1,2n+1}^* \\ x_{2,2n} \\ -x_{2,2n+1}^* \end{bmatrix} + n_{1,2n} \\ r_{1,2n+1} &= [\, h_{1,1} \quad h_{1,2} \quad h_{1,3} \quad h_{1,4} \,] \cdot \begin{bmatrix} x_{1,2n+1} \\ x_{1,2n}^* \\ x_{2,2n+1} \\ x_{2,2n}^* \end{bmatrix} + n_{1,2n+1} \end{aligned} \tag{48}$$

And for R

$$\begin{aligned} r_{2,2n} &= [\, h_{2,1} \quad h_{2,2} \quad h_{2,3} \quad h_{2,4} \,] \cdot \begin{bmatrix} x_{1,2n} \\ -x_{1,2n+1}^* \\ x_{2,2n} \\ -x_{2,2n+1}^* \end{bmatrix} + n_{2,2n} \\ r_{2,2n+1} &= [\, h_{2,1} \quad h_{2,2} \quad h_{2,3} \quad h_{2,4} \,] \cdot \begin{bmatrix} x_{1,2n+1} \\ x_{1,2n}^* \\ x_{2,2n+1} \\ x_{2,2n}^* \end{bmatrix} + n_{2,2n+1} \end{aligned} \tag{49}$$

To recover the transmitted data, we can form the receive vector: $[\mathrm{r}_{1,2n}\mathrm{r}_{1,2n+1}^* \; \mathrm{r}_{2,2n}\mathrm{r}_{2,2n+1}^*]^T$. This can be written as:

$$\begin{bmatrix} r_{1,2n} \\ r_{1,2n+1}^* \\ r_{2,2n} \\ r_{2,2n+1}^* \end{bmatrix} = \begin{bmatrix} h_{1,1} & -h_{1,2} & h_{1,3} & -h_{1,4} \\ h_{1,2}^* & h_{1,1}^* & h_{1,4}^* & h_{1,3}^* \\ h_{2,1} & -h_{2,2} & h_{2,3} & -h_{2,4} \\ h_{2,2}^* & h_{2,1}^* & h_{2,4}^* & h_{2,3}^* \end{bmatrix} \cdot \begin{bmatrix} x_{1,2n} \\ x_{1,2n+1}^* \\ x_{2,2n} \\ x_{2,2n+1}^* \end{bmatrix} + \begin{bmatrix} n_{1,2n} \\ n_{1,2n+1}^* \\ n_{2,2n} \\ n_{2,2n+1}^* \end{bmatrix} \tag{50}$$

From the above equation, we can see that the first two columns and last two columns are orthogonal. This shows there is no interference between $x_{1,2n}$, $x_{1,2n+1}^*$, as well as between $x_{2,2n}$, $x_{2,2n+1}^*$. However, there is still interference between $x_{1,2n}$ and $x_{2,2n}$ (spatial division multiplexing). MIMO detection, based on the forms for the receive vector, channel matrix shown above, can be used to recover the spatial streams.

III.2.4 Transmit Beamforming

Transmit beamforming is a technique where channel estimates are used to find the spatial matrices for signal transmission, where the goal is to improve receive signal strength by emphasizing the dominant modes of transmission for the channel. It is known, from an information-theoretical perspective, that the use of singular value decomposition (SVD) for this process is optimal [21], and also results in channel diagonalization (described later), which simplifies MIMO detection.

For beamforming, we can consider that, from [9], [22], the SVD decomposition can be written in the following form:

for any N_{RX}-by-N_{TX} matrix, H_k:

$$H_k = U_k \Sigma_k V_k^H \tag{51}$$

where:

- H_k is a matrix of channel estimates for sub-carrier k,
- $\sum_k$ is a diagonal matrix of "singular values," $\sigma_0, \sigma_1, \ldots \sigma_{N-1}$ which are real and non-negative,
- U_k is an N_{RX}-by-N orthonormal matrix,
- V_k is an N_{TX}-by-N orthonormal matrix,
- N is $\min\{N_{RX}, N_{TX}\}$.

Note that the SVD decomposition can equivalently be written with the singular values of $\sum_k$ in descending order, by reordering the associated columns of U_k, V_k. Based on the above decomposition, the optimal choice for spatial matrices is V_k. With this choice for beamforming, the received signal can be written as (considering $V_k^H V_k = I$, since V_k is an orthonormal matrix):

$$\begin{aligned} r_k &= H_k V_k x_k + n_k \\ &= U_k \Sigma_k V_k^H V_k x_k + n_k \\ &= U_k \Sigma_k x_k + n_k \end{aligned} \tag{52}$$

Thus, we can see that the singular values on the diagonal of $\sum_k$ represent the received signal strength for the corresponding element, x_k, (i.e., transmitted symbol on spatial stream, k) at the receiver. This becomes clearer when we consider, with the matched filter, U_k^H, at the receiver:

$$\begin{aligned} y_k &= U_k^H r_k \\ &= U_k^H (U_k \Sigma_k x_k + n_k) \\ &= \Sigma_k x_k + U_k^H n_k \end{aligned} \tag{53}$$

With the singular values organized in descending order, the spatial streams have descending receive signal strengths. Thus, if less spatial streams are used, the first N_{SS} columns of V_k can be used, corresponding to the largest singular values (receive signal strengths). The column vectors of V_k are commonly referred to as eigenmodes, or singular modes, of the channel.

With the first N_{SS} columns of V_k written as $[V_k]_{Nss}$, we can write:

$$\begin{aligned} r_k &= H_k [V_k]_{Nss} x_k + n_k \\ &= U_k \Sigma_k V_k^H [V_k]_{Nss} x_k + n_k \\ &= [U_k \Sigma_k]_{Nss} x_k + n_k \end{aligned} \tag{54}$$

Note that with the choice of V_k for the beamforming spatial matrices, and U_k^H for the receiver matched filter, the channel becomes completely diagonalized, which simplifies ML detection (see MIMO detection, space-time block coding for details).

There are two basic approaches for beamforming: implicit and explicit beamforming [8]:

With *explicit beamforming*, the remote side sends either its channel estimates or pre-computed spatial matrices to the transmit station for beamforming.

With *implicit beamforming*, the transmitting station uses the transpose of its own channel estimates as an estimate of the remote side channel estimates. This is based on the assumption that the channel response from the transmitting station's antenna, j, to the remote side's antenna, k, is the same as the channel response in the reverse path, with the remote side transmitting. This channel property is known as channel reciprocity [9].

Note, however, that channel reciprocity only applies to the actual "over-the-air" signal transmission, and that channel reciprocity is not observed in practice, due to differences in the attenuation, delays of the Tx and Rx antenna chains for the two stations. Thus, before implicit beamforming can be performed, a calibration process is required to correct for the Tx, Rx chain differences.

With the actual "over-the-air" channels (between stations A, B) written as:

$$H_{k,A->B} = H_{k,B->A}^T \tag{55}$$

the observed channels for stations A and B (considering Tx, Rx chains of both stations) can be written as [9]:

$$\begin{aligned} \widetilde{H}_{k,A->B} &= C_{k,B:Rx} H_{k,A->B} C_{k,A:Tx} \\ \widetilde{H}_{k,B->A} &= C_{k,A:Rx} H_{k,B->A} C_{k,B:Tx} \end{aligned} \tag{56}$$

where $C_{k,A:Tx}$, for example, is the Tx chain amplitude, phase response for station A (assumed to be a diagonal matrix).

As described previously, the observed channels generally do not exhibit reciprocity. However, correction factors may be added to restore reciprocity. For the observed channels to exhibit reciprocity, correction factors are chosen to satisfy:

$$\left(\widetilde{H}_{k,A->B}K_{k,A}\right) = \left(\widetilde{H}_{k,B->A}K_{k,B}\right)^T \tag{57}$$

where $K_{k,A}$ is the correction factor applied to the transmitter of station A, and $K_{k,B}$ is the correction factor applied to the transmitter of station B.

Channel reciprocity is restored with correction factors:

$$\begin{aligned} K_{k,A} &= C^{-1}_{k,A:Tx}C^{T}_{k,A:Rx} \\ K_{k,B} &= C^{-1}_{k,B:Tx}C^{T}_{k,B:Rx} \end{aligned} \tag{58}$$

Since:

$$\begin{aligned} \left(\widetilde{H}_{k,A->B}K_{k,A}\right) &= C_{k,B:Rx}H_{k,A->B}C_{k,A:Tx}C^{-1}_{k,A:Tx}C^{T}_{k,A:Rx} \\ &= \left(C_{k,B:Rx}H_{k,A->B}C^{T}_{k,A:Rx}\right) \end{aligned} \tag{59}$$

and:

$$\begin{aligned} \left(\widetilde{H}_{k,B->A}K_{k,B}\right)^T &= C_{k,B:Rx}\left(C^{-1}_{k,B:Tx}\right)^T \\ &\quad \times C^{T}_{k,B:Tx}H^{T}_{k,B->A}C^{T}_{k,A:Rx} \\ &= \left(C_{k,B:Rx}H_{k,A->B}C^{T}_{k,A:Rx}\right) \end{aligned} \tag{60}$$

III.2.5 MIMO Channel Estimation

Here we describe general approaches for MIMO channel estimation. The focus is mostly on frequency-domain techniques, as well as illustrating the process of channel estimation using least-squares.

From the channel model given previously, with the use of OFDM and cyclic prefix, the channel can be written as (in the frequency domain):

$$R(k) = H(k)S(k) + N(k) \tag{61}$$

where $H(k)$, for a MIMO channel, is:

$$H(k) = \begin{bmatrix} h_{1,1}(k) & \cdots & h_{1,M}(k) \\ \vdots & \ddots & \vdots \\ h_{N,1}(k) & \cdots & h_{N,M}(k) \end{bmatrix} \tag{62}$$

and the elements $h_{i,j}$ are each complex scalar values representing the channel gain, phase, from transmit antenna j to receive antenna i for sub-carrier k.

Before describing the process for MIMO channel estimation, first consider the SISO (single-input, single-output) case. For a SISO system, the received symbol r_k can be written as:

$$r_k = H_k s_k + n_k \tag{63}$$

With SISO, obtaining a least-squares channel estimate for sub-carrier k only requires multiplying the received symbol by the conjugate of the transmitted symbol (since all training symbols s_k are constrained to unit magnitude). Thus, the channel estimates are:

$$\begin{aligned} \hat{H}_k &= r_k s_k^* \\ &= (H_k s_k + n_k) \cdot s_k^* \\ &= H_k |s_k| + n_k s_k^* \end{aligned} \tag{64}$$

Note that the training pattern, s_k, across sub-carriers, for all proposals under study, is a sign pattern with unit magnitude. The pattern used is similar to the one used in IEEE 802.11a. An example is shown in (65) at the bottom of the page.

In order to extend the channel estimation for MIMO, the training pattern is coded across dimensions other than frequency: time (OFDM symbols) and space (transmit antennas). In addition, other techniques (such as temporal diversity) may also be used.

For MIMO channel estimation with the current IEEE 802.11n draft, in addition to frequency sub-carrier, the long training field (HT-LTF) is encoded over space and time. The following orthogonal matrix is used [8]:

$$P_{HTLTF} = \begin{bmatrix} 1 & -1 & 1 & 1 \\ 1 & 1 & -1 & 1 \\ 1 & 1 & 1 & -1 \\ -1 & 1 & 1 & 1 \end{bmatrix} \tag{66}$$

For the above training sequence matrix, the rows represent space (different spatial streams), while the columns represent time (OFDM symbols). The same training matrix is used for every sub-carrier k.

$$HTLTF_{-28:28} = \begin{bmatrix} 1,1,1,1,-1,-1,1,1,-1,1,-1,1,1,1,1,1,1,-1,-1,1,1,-1,1,-1,1,1,1,1,0, \\ 1,-1,-1,1,1,-1,1,-1,1,-1,-1,-1,-1,-1,1,1,-1,-1,1,-1,1,-1,1,1,1,1,-1,-1, \end{bmatrix} \tag{65}$$

To separate the spatial streams at the receiver, the orthogonality of the rows is used. Considering that the transmitted training sequence is the columns of P_{HTLTF} sent over different OFDM symbols, we can represent the received training sequence for subcarrier k in a matrix form (call this matrix $R_{HTLTF,k}$), where the i-th column of $R_{HTLTF,k}$ is the received training sequence for OFDM symbol i.

The received sequence, in matrix form, can be written as:

$$R_{HTLTF,k} = H_k(S_k P_{HTLTF}) + N_k \tag{67}$$

where $S_k \cdot P_{HTLTF}$ is the transmitted training sequence for sub-carrier, k, over all OFDM symbols.

To obtain a least-squares estimate of the MIMO channel, we can write:

$$\begin{aligned} R_{HTLTF,k}W_{HTLTF} &= H_k\,(S_k P_{HTLTF})\,W_{HTLTF} \\ &\quad + N_k W_{HTLTF} \\ &= H_k + N_k W_{HTLTF} \end{aligned} \tag{68}$$

where $W_{HTLTF} = U^H(UU^H)^{-1}$ (pseudo-inverse of $U = S_k P_{HTLTF}$). But since S_k is either $+1$ or -1:

$$W_{HTLTF} = S_k P_{HTLTF}^H \left(P_{HTLTF} P_{HTLTF}^H\right)^{-1} \tag{69}$$

Thus, we only need to consider the pseudo-inverse of P_{HTLTF} in finding the least-squares channel estimate (the S_k term can be handled separately). Also, note that since all rows of P_{HTLTF} are orthogonal, each with same norm (vector magnitude), the pseudo-inverse is simply its transpose with a scaling factor (the inverse of the norm squared).

For different numbers of spatial streams (N_{STS}),the training sequence patterns, pseudo-inverse matrices are:

$$\begin{aligned} P_{Nsts} &= [P_{HTLTF}]_{NSTS,NDLTF} \\ W_{Nsts} &= S_k \frac{1}{N_{STS}} P_{Nsts}^T \end{aligned} \tag{70}$$

where the notation $[A]_{NSTS,NDLTF}$ denotes the first N_{STS} rows, N_{DLTF} columns of matrix A, and N_{DLTF} is the number of OFDM training symbols. And the least-squares channel estimate is:

$$\begin{aligned} \hat{H}_k &= R_{Nsts,k}W_{Nsts} \\ &= H_k + N_k W_{Nsts} \end{aligned} \tag{71}$$

Note that in the above, the number of streams used for training is the number of space-time streams (N_{STS}), since the use of additional spatial streams

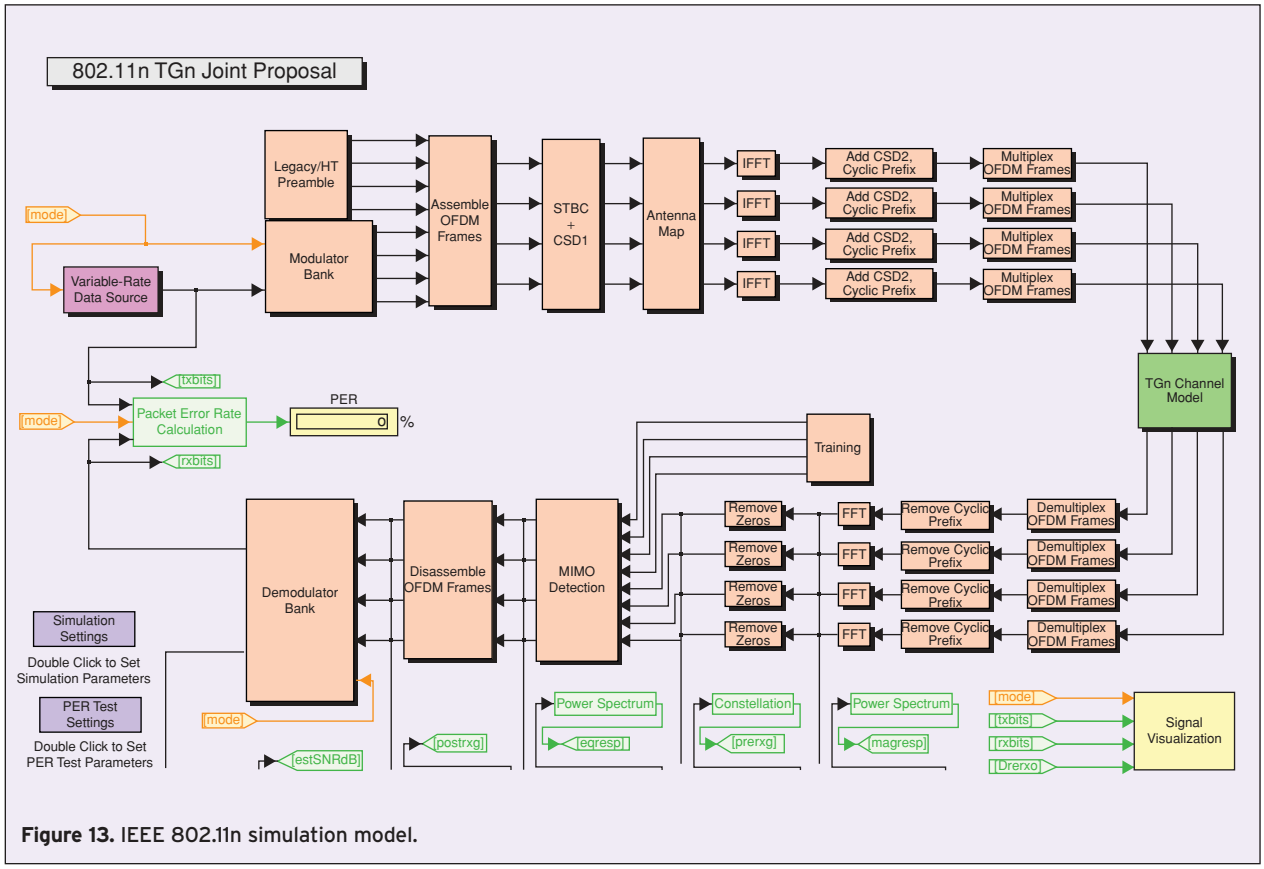

Figure 13. IEEE 802.11n simulation model.

with space-time block coding (STBC) requires channel estimates for these streams (see subsection describing the space-time block coding).

IV. Performance of IEEE 802.11n PHY

In this section, a simulation model in MATLAB/SIMULINK is used to illustrate the performance of the PHY described in the IEEE 802.11n amendment. The simulation model described in this paper was developed and based on the IEEE 802.11a simulation model by Martin Clark available on MATLAB Central [23]. A high level block diagram of the 11n simulation model is shown in Figure 13.

For the performance tests, the following settings were used:

- Receiver type: MMSE detector,
- Payload Size: 1000 bytes,
- AWGN, Ch D (nLOS) channels (no impairments),
- Per-tone channel est. (no smoothing).

The following configurations were tested:

Fig. 14: AWGN, 2x2 Direct-map,
Fig. 15: Ch D (nLOS), 2x2 Direct-map,
Fig. 16: Ch D (nLOS), 2x2 Beamforming,
Fig. 17: Ch D (nLOS), 4x2 STBC.

The PER (packet error rate) vs. SNR results are shown below.

The PER curves in Figure 14 show the performance of the 11n PHY and an Additive White Gaussian Noise (AWGN) channel. The curves should directly reflect the Modulation and Coding Settings (MCS) settings used (MCS 13–15—see [5] for details). Note these modulation settings are similar to 802.11a/g.

In Figure 15 (Channel D, nLOS), a delay spread channel (reflecting a typical office-type environment) is simulated, leading to frequency-selective fading. For this type of channel, the SNR varies across data carriers, and the PER is dominated by the low SNR carriers. Thus, a higher average SNR is required to achieve the same PER as for the AWGN channel.

Figure 16 shows the benefit of beamforming (use of eigenmodes for transmission). Note that the gain is modest (only around 2 dB), since same number of Tx antennas as spatial streams is used (2x2 MIMO). Thus, the diversity order is not increased. The benefit originates solely from channel diagonalization (i.e., use of orthogonal transmission modes). Since Ch D (nLOS) is a Rayleigh fading MIMO channel, the benefit of diagonalizing channel is modest.

Finally, Figure 17 shows the benefit of 4x2 STBC (2 spatial streams, 4 space-time streams). Note the significant improvement (about 8 dB) compared to 2x2 direct-map and beamforming, due to the additional transmit diversity order, which is used to provide STBC coding for each of the transmitted spatial streams.

In order to compare better the various PHY configurations for the IEEE 802.11n amendment, Figure 18 shows simulation results of the average throughput versus distance under an office-type environment (Channel D). Note, for each of these tests, that the focus is on PHY layer performance, and the influence of the MAC layer on throughput (also considering frame aggregation) was approximated to provide suitable results.

The following IEEE 802.11 PHY layer configurations were tested:

- IEEE 802.11a/g (as reference),
- SISO,
- 2x1 STBC,
- 2x2 SDM,
- 2x2 SDM + Beamforming,

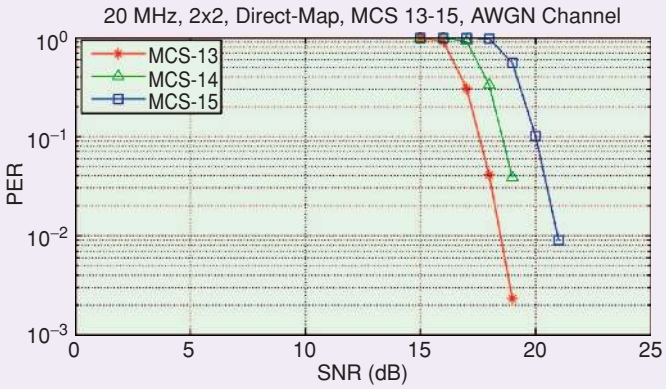

Figure 14. IEEE 802.11n PHY: AWGN, 2x2 Direct-Map.

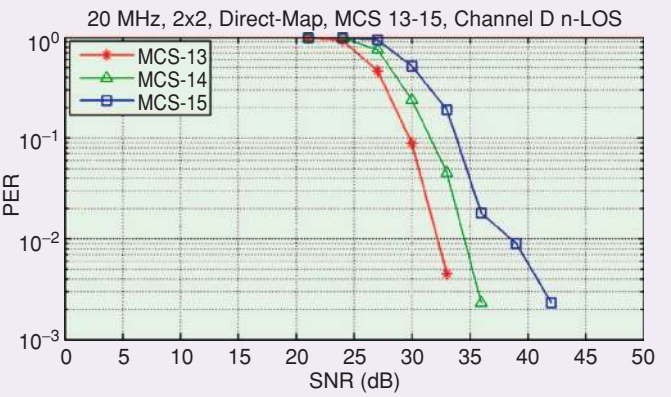

Figure 15. IEEE 802.11n PHY: Ch D, nLOS, 2x2 Direct-Map.

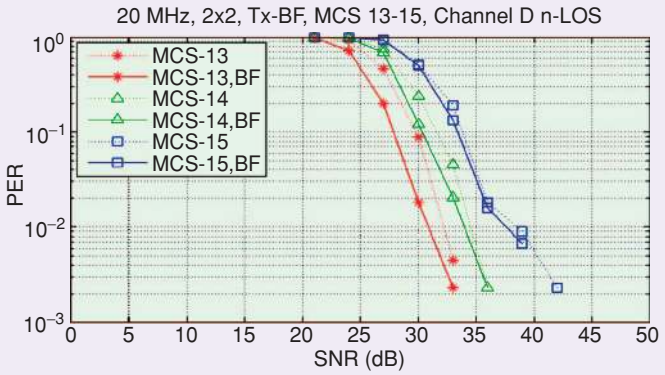

Figure 16. IEEE 802.11n PHY: Ch D, nLOS, 2x2 beamforming.

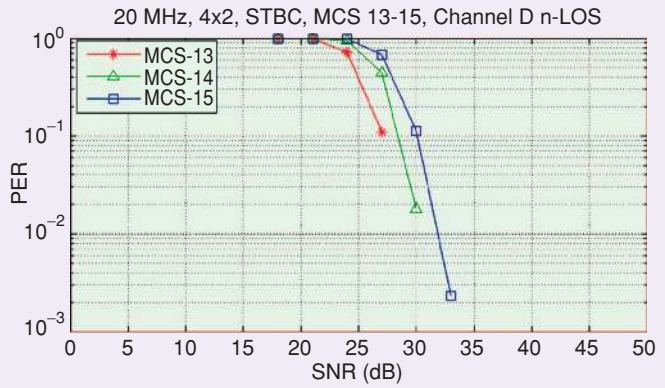

Figure 17. IEEE 802.11n PHY: Ch D, nLOS, 4x2 STBC.

- 4x2 STBC,
- 4x4 SDM + Beamforming.

The graphs show the increase in throughput obtained using multiple spatial streams (the last four PHY configurations). For the 2x2 and 4x4 tests, we see that the throughput is generally double (or four times with 4x4) that of the SISO case for shorter distances (less than 20 m). However, at larger distances, note that the 2x2 SDM throughput reduces to levels similar to SISO, and below 2x1 STBC. This is due to the fact that, at these distances, the low SNR affects MIMO detection (note that MIMO detection balances noise whitening, interference cancellation), resulting in a reduced ability to perform interference cancellation for the spatially-multiplexed streams. Moreover, the performance is slightly better for 2x2 SDM with beamforming, as the use of orthogonal transmission modes improves the signal strength at the receiver.

However, for the results with 2x2 SDM with beamforming, the overall performance gain is modest (less than 5 Mbps), for the same reasons described previously for Figure 16. Finally, regarding the use of 4x2 STBC, the general performance benefit over both the 2x2 SDM and 2x2 SDM + beamforming tests, again due to the additional transmit diversity order.

One final area to consider is the performance of the 802.11a/g baseline. We see that, at close distances, the performance of the 11a/g baseline is around half that of the IEEE 802.11n SISO. This is mainly due to the frame aggregation used with 11n (see [6]), which allows the practically achievable throughput to approach the actual PHY data rate. At larger distances, however, the performance gap between the 11a/g and the 11n SISO case reduces considerably. This is due to the fact that very low data rates are used at this range significantly increasing the packet duration (the data portion of the packet), thus reducing overhead as well as the need for frame aggregation. However, even at large distances, some benefit from the use of frame aggregation can be observed.

From the above tests, we can see the benefits provided by the IEEE 802.11n PHY layer, in terms of both range and throughput, over the 11a/g PHY. We also note that the use of frame aggregation was required to reduce packet overhead sufficiently to achieve throughputs approaching the PHY rate (we can compare the 11a/g and 11n SISO results to observe this).

V. Considerations for Rapid Hardware Prototyping

For many companies, the ability to develop rapidly hardware prototypes of potential system designs is essential. Rapid prototyping enables designers to bring-up quickly working systems for evaluation, allowing them to debug fully system issues before investing significant effort in the ASIC design process. In this section, we discuss considerations for rapid hardware prototyping, focusing on a MATLAB-based FPGA design flow, with the Xilinx Virtex-4 FPGA as a potential platform.

The use of MATLAB considerably simplifies the system design task, providing an environment well suited to the mathematical nature of the algorithms involved, as well as providing extensive toolboxes (i.e., Signal Processing Toolbox, Communications Toolbox, etc) for rapid algorithm development. The use of SIMULINK in MATLAB further simplifies the design process by providing a graphical environment where designers can put together pre-designed blocks from various blocksets (similar to toolboxes), to create block diagrams of system designs which can be fully simulated for algorithm verification.

For rapid prototyping for FPGAs, Xilinx provides the System Generator Blockset for SIMULINK: a library of prebuilt blocks, ranging from the elementary (such as block RAMs, MUXes) to more complex blocks (such as Viterbi,

FFT). Use of these pre-built blocks should allow for efficient utilization of the available resources within the Virtex-4.

Alternatively, the AccelDSP Synthesis tool by AccelChip provides an interface to the Xilinx System Generator, and gives developers the flexibility to develop custom system architectures for FPGAs directly from a floating-point MATLAB design. Interested readers can refer to [24] for details.

The Xilinx Virtex-4 family of FPGAs provides the following [25]:

- Up to 512 XtremeDSP slices (500 MHz), for 256 Billion MACs/s,
- Low power consumption: 23 uW/MHz per XtremeDSP slice,
- Up to 200,000 logic cells
  - provides high-speed carry logic for math-intensive applications,
  - Lookup tables configurable as logic, RAM, or shift registers,
  - Up to IBM PowerPC 32-bit RISC Processor with APU Controller
  - 680 DMIPS @ 450 MHz,
  - single FPGA can support two processors for 1360 DMIPS.

At this point, we present some design strategies to consider in the hardware prototyping of a design for FPGA. Note, however, that the development of a hardware prototype is not the focus of the work described in this article, and this section is only meant to serve as a guide regarding hardware prototyping issues.

In rapid hardware prototyping for FPGAs, the main areas of focus are the speed of system bring-up, fitting the design onto the FPGA, and system functionality. Issues such as power consumption or minimizing gate count are not primary concerns.

Thus, a key issue in the development of an 11n system prototype is the tradeoff between FPGA resource utilization and design parallelism for meeting clock requirements. The available XtremeDSP slices (up to 512, depending on the chip model) should be utilized in a reasonably efficient fashion in performing the various DSP algorithms described in Section III (MIMO detection, channel estimation, STBC, beamforming, etc).

Assuming the use of the maximum clock rate of 500 MHz, and considering the required baseband sampling rate (20 MHz), we see that 512*(500/20) = 12800 MAC operations can be performed per sample, or 12800*80 = 1M MACs per OFDM symbol. Note, however, that accommodating the critical paths associated with a design of the complexity of an 802.11n system generally requires the use of a significantly lower clock rate (for example, around 160 MHz). In this case, we have: 512*(160/20) = 4096 MACs per sample, or 4096*80 = 327,680 MACs per OFDM symbol.

In order to maximize generally the achievable clock rate, pipelining is a common approach [13]. Pipelining involves dividing the stages of combinational logic in a design using registers, in an effort to reduce the critical path. Pipelining results in a slight increase in logic gates (from adding registers) as well as an increase in output latency (due to buffering with registers).

Another approach to improve the clock rate is reducing fanout. Fanout refers to the number of load gates connected to the output of a driving gate [13]. With a large fanout, the driving gate output can become degraded, reducing the reliability of the output at higher clock rates. The use of buffers between the driving and load gates can be used to reduce fanout, and improve the system performance at higher clock rates.

Regarding the above issues, note that the use of Xilinx System Generator simplifies these areas of the design, as the blocks provided with System Generator contain the required registers for pipelining, which may be enabled or disabled, depending on design consideration.

In the design of any complex system, one typical area for optimization is module reuse. Module reuse in FPGA designs can be used to minimize resource allocation. Modules in an 802.11n system which may be reused include the FFT/IFFT (which can be shared between the transmitter, receiver) and SVD decomposition (can be used for determining beamforming matrices, and well as channel matrix inversion). However, module reuse is

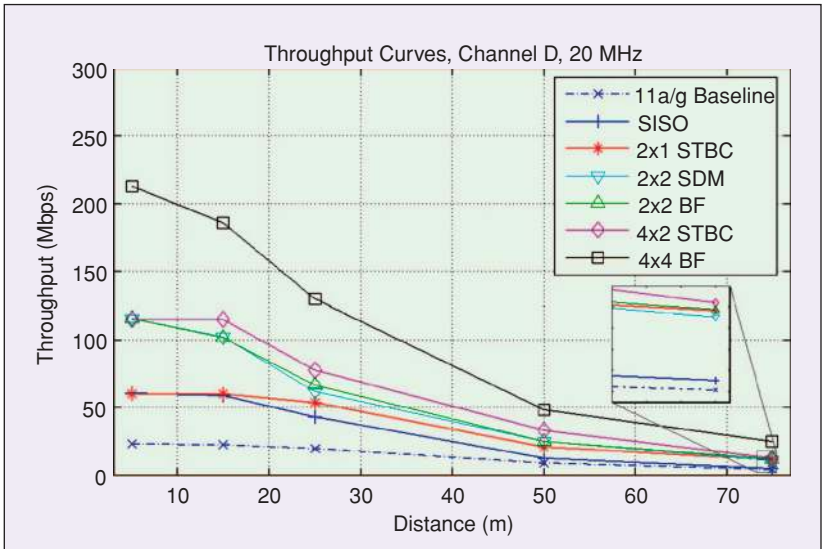

Figure 18. IEEE 802.11n PHY: Throughput vs. Ch D, Various Config.

contingent on whether sufficient clock cycles exist to complete the required processing.

The above techniques should serve as good hardware design practices in general, and minimize the effort required for a successful FPGA design flow.

VI. Future Trends

Currently, the IEEE 802.11n standard is still in the draft stage, and is expected to be finalized in 2008. As of October 2007, Draft 3.0 has been released, addressing over 1000 comments made regarding Draft 2.0, and providing revisions for areas such as security establishment, Clear Channel Assessment (CCA) as well as MAC layer management of channel switching and PHY features (LDPC, STBC, etc.).

Although the IEEE 802.11n PHY provides many benefits over the IEEE 802.11a/b/g standards, most notably in throughput (i.e., spectral efficiency) as well as range, one drawback is the increased potential for interference with other radio-based systems operating in the ISM band (2.4 GHz to 2.4835 GHz).

Of interest is the interoperability of IEEE 802.11n and Bluetooth products, which are also based on a 2.4 GHz carrier. The Bluetooth standard uses FHSS modulation, randomly hopping across 79 different frequency locations (with 1 MHz spacing) 1600 times a second, to avoid interference. Bluetooth is used to establish personal-area networks (PANs) for devices such as keyboards, mice, headsets, etc., where the device is typically within ten meters of the PC.

Considering the improved spectral efficiency of IEEE 802.11n, in addition to the optional use of 40 MHz bandwidth (essentially occupying half the ISM band), the interference provided with this new standard is substantially higher than with the 11a/g solutions. Also, although Bluetooth devices (starting with Bluetooth 1.2) use a scheme known as adaptive frequency hopping (AFH) to detect and avoid interference, if both devices are present within the same PC or handheld device (referred to as being co-located), the significantly high signal strength of the WLAN signal can impair the signal detection capability of the Bluetooth device [26]. Note that the WLAN transmitted signal power is typically much higher than the Bluetooth, since the desired range of operation is much larger—around 100 m, although higher transmit powers may be used for Bluetooth to support these types of distances as well [27].

As an alternative, the use of the clear channel assessment (CCA) indicator with IEEE 802.11n can help reduce interference with Bluetooth, since this allows the WLAN device to delay transmission until the 'over-the-air' channel is clear. However, interoperability of IEEE 802.11n and Bluetooth still remains an area of ongoing research.

Also of interest are the similarities between the IEEE 802.11n standard and IEEE 802.16, also known as WiMAX. The frequency ranges being considered for WiMAX are all outside the ISM band. World-wide, the bands under consideration for WiMAX are 2.3 GHz, 2.5 GHz, 3.5 GHz, and 5.7 GHz [28]. For North America, the band allocated for WiMAX is 2.495 GHz to 2.690 GHz, known as the Broadband Radio Services (BRS) band. Thus, the direct signal interference between the IEEE 802.11 and IEEE 802.16 PHY layers should be minimal and, in the worst-case, similar to the interference between two adjacent 802.11 channels.

Regarding the usage models intended for 802.11n and WiMAX, it appears clear that there may be a conflict, as both products provide broadband wireless internet access to the end user, and are designed for use in PCs and handheld devices.

The main differences between the two standards, however, are the service area and throughput. IEEE 802.16 provides service within a metropolitan area (up to 2 miles for mobile WiMAX, and 5 miles for fixed WiMAX), whereas IEEE 802.11 is used to establish local-area networks (typical distances up to 200 feet indoors). Meanwhile, WiMAX offers downstream throughputs ranging from 1 Mbps up to 46 Mbps (with IEEE 802.16e, 2x2 MIMO, 10 MHz bandwidth), while IEEE 802.11n provides throughputs exceeding 200 Mbps.

In addition to the differences described above, the IEEE 802.16 standard is also designed to support many diverse features, such as use of both FDD and TDD for multi-user bandwidth allocation Orthogonal Frequency Division Multiple Access (OFDMA), seamless handovers for mobile applications (with mobile WiMAX—also designed for robustness against large Doppler spreads), HARQ (Hybrid automatic repeat request—use of retransmission with error control, so the retransmitted packet can be combined with the original packet to improve receive reliability) as well as robust security features [28], [29].

From the above considerations, the roles of IEEE 802.16 for general metro-wide broadband internet (with mobility), and IEEE 802.11n for indoor (home or office) high-throughput internet access seem distinct and well-defined, and would appear most likely to remain so for many years to come.

VII. Conclusions

The IEEE 802.11n amendment contains numerous modifications to the IEEE 802.11 standard, which were outlined here. The changes are mostly focused on extending throughput and range with the 802.11 standard, and include:

For the media access control (MAC) layer:

- Additions for frame aggregation, block acknowledgments, a reverse-direction (RD) data protocol, changes to support co-existence with legacy devices, as well as improvements for QoS, and other changes.

For the physical (PHY) layer:

- Addition of MIMO techniques (spatial-division multiplexing, space-time block coding, beamforming, etc.), channel bonding (40 Mhz mode), and advanced coding (LDPC).

The changes to the PHY layer were the focus of our discussion, which included a description of the MIMO channel model, covering areas such as large-scale path loss (i.e., average loss in signal strength over distance) and small-scale fading effects (for example, fading effects caused by travelling short distances, i.e., time-selective fading), as well as the benefits of OFDM. These are described in detail in Subsection III.1.1 and III.1.2.

Further elaborating on the MIMO channel, Subsection III.1.3 described the approach for MIMO channel modeling used for the TGn Channel models, which are more advanced MIMO channel models suitable for 802.11n PHY performance characterization. This approach involves modeling the MIMO channel using a set of clusters (i.e., reflection paths, each with some scattering effects). With this approach, we were able to describe the line-of-sight (LOS) and non line-of-sight (NLOS) components of a MIMO channel, the effect of the Doppler components of channel (resulting in frequency dispersion, random AM distortions, depending on the component), as well as the expected signal correlation across the antenna arrays. This is based on the configuration of the transmitting and receiving WLAN devices, surrounding environment.

Afterwards, we described the various MIMO techniques used at the receiver for achieving the high throughput and range proposed with the 802.11n PHY layer. The approaches described include:

Spatial-division multiplexing (SDM):

- transmission of parallel data streams across antennas for increased data rates (if suitable for channel),

Space-Time Block Coding (STBC):

- coding across antennas (space), OFDM symbols (time), at the transmitter to improve diversity, reduce fading at receiver,

Transmitter beamforming:

- use of the orthogonal transmission modes of channel to maximize the signal strength at receiver, minimize signal interference between spatial streams with SDM (if used).

Note that techniques for MIMO detection as well as channel estimation, were also considered in Subsection III.2.

To illustrate the benefits of the use of MIMO as well as the advantages of the modifications to the PHY layer proposed with IEEE 802.11n various simulation results were presented in Section IV. The first set of results show the performance of some system configurations, in terms of packet error rate (PER) versus signal-to-noise (SNR). The system configurations for these tests consist of 2x2 SDM, 2x2 SDM with beamforming, and 4x2 STBC. These tests allow for a performance comparison of the different MIMO techniques described (constrained to use of two spatial streams). For additional information regarding the performance of these MIMO techniques as well as a comparison of the initial proposals for the 11n standard (the TGn Sync, WWiSE, and TGn Joint proposals), the reader can refer to [30].

In Section IV, we also showed a performance comparison of several 11n configurations, and the performance under 11a/g, in terms of average throughput versus distance. The 802.11n configurations tested consisted of SISO, 2x1 STBC, 2x2 SDM (with/without beamforming), 4x2 STBC, and 4x4 SDM (with beamforming). This test also considered the MAC enhancements required for achieving throughputs approaching the PHY data rate. The benefits of 11n, both in achieving this ideal throughput as well as in providing effective throughputs on the order of ten times higher than 11a/g, were shown in this section. Note that these tests do not consider the use of channel bonding (40 MHz mode), which would effectively double the 11n throughput results.

In Section V, we discussed some considerations for rapid hardware prototyping of a potential 11n baseband design. Possible MATLAB-based FPGA design flows were discussed as well as the available resources with the Xilinx Virtex-4 family of FPGAs. In addition, various design considerations for rapid prototyping such as pipelining, reducing fanout, etc. were described.

Finally, in Section VI, we considered the future trends for wireless LAN, mostly focusing on the co-existence of 11n-based products with Bluetooth and WiMAX. Regarding co-existence with Bluetooth, the shared use of the ISM band (2.4–2.4835 GHz) clearly creates interoperability issues between the two types of devices, particularly when they are co-located. The frequency hopping used by Bluetooth does not provide significant protection from interference with 11n products, particularly considering the improved efficiency (i.e., reduced overhead as well as spectral efficiency), and the potential use of 40 MHz mode, consuming half the ISM band. Interoperability with Bluetooth is an area of ongoing research, and is vital for the mutual success of the two technologies.

Regarding the co-existence of 802.11n products with WiMAX, although the two standards describe the use of separate frequency bands (resulting in minimal signal interference), co-existence is still a concern due to the similarity of many aspects of the respective usage models (discussed in detail in Section V). The key differences between the two standards are in the intended service areas (a range of around 200 feet with 802.11n, versus 2 to 5 miles with WiMAX), resulting in significant differences in the PHY layer and MAC layer architectures, which should allow for co-existence of the two technologies in the marketplace.

VIII. References

[1] A. Molisch, "*Wireless Communications*," Wiley, West Sussex, 2005.
[2] A. Goldsmith, "*Wireless Communications*," Cambridge, New York, 2005.
[3] B. O'Hara and A. Petrick, "*IEEE 802.11 Handbook*," 2nd ed. IEEE Press, New York, 2005.
[4] J. Farwell, "Wi-Fi on Steroids," *PC Today*, July 2006.
[5] IEEE P802.11n/D3.00, Wireless LAN Medium Access Control (MAC) and Physical Layer (PHY) specifications: Amendment 4: Enhancements for Higher Throughput.
[6] Y. Xiao, "IEEE 802.11n: Enhancements for Higher Throughput in Wireless LANs," *IEEE Wireless Communications*, Dec. 2005.
[7] *TGn Channel Models*, IEEE Std. 802.11 – 03/940r4, May, 2004. Available: http://www.ieee802.org/11/DocFiles/03/11-03-0940-04-000n-tgn-channel-models.doc
[8] *Joint Proposal: High throughput extension to the 802.11 Standard: PHY doc.:* IEEE 802.11-05/1102r4. Available: http://www.ieee802.org/11/DocFiles/05/11-05-1102-04-000n-joint-proposal-phy-specification.doc
[9] *TGn Sync Proposal Technical Specification document:* IEEE 802.11-04/0889r7. Available: http://www.ieee802.org/11/DocFiles/04/11-04-0889-07-000n-TGn Sync-proposal-technical-specification.doc
[10] *WWiSE Proposal: High throughput extension to the 802.11 Standard*: IEEE 802.11-05/0149r5. Available: http://www.ieee802.org/11/DocFiles/05/11-05-0149-05-000n-wwise-proposal-high-throughput-extension-to-802-11-standard.doc
[11] T.S. Rappaport, "*Wireless Communications: Principles and Practice*," 2nd Ed., Prentice Hall, New Jersey, 2002.
[12] J. Barry, E. Lee, and D. Messerschmitt, "*Digital Communications*," 3rd ed. New York: Springer, 2004.
[13] J. Terry and J. Heiskala, "*OFDM Wireless LANs: A Theoretical and Practical Guide*," Indianapolis: Sams, 2002.
[14] H. Yang, "A Road to Future Broadband Wireless Access: MIMO-OFDM-Based Air Interface," *IEEE Communications Magazine*, Jan. 2004.
[15] G.L. Stuber, J.R. Barry, S.W. McLaughlin, Y. Li, M.A. Ingram, and T.G. Pratt, "Broadband MIMO-OFDM Wireless Communications," *Proceedings of the IEEE*, vol. 92, no. 2, pp. 271–294.
[16] A. Saleh and R. Valenzuela, "A statistical model for indoor multipath propagation," *IEEE Journal of Selected Areas in Communications*, vol. SAC 5, no. 2, pp. 138–146, Feb. 1987.
[17] Q.H. Spencer, et al., "Modeling the statistical time and angle of arrival characteristics of an indoor environment," *IEEE Journal of Selected Areas in Communications*, vol. 18, no. 5, pp. 561–570, May 2002.
[18] L. Schumacher, K.I. Pedersen, and P.E. Mogensen, "From antenna spacings to theoretical capacities – guidelines for simulating MIMO systems," in *Proc. PIMRC Conf.*, vol. 2, Sept. 2002, pp. 587–592.
[19] J.P. Kermoal, L. Schumacher, P.E. Mogensen, and K.I. Pedersen, "Experimental investigation of correlation properties of MIMO radio channels for indoor picocell scenarios," in *Proc. IEEE Vehicular Technology Conference*, Boston, USA, vol. 1, Sept. 2000, pp. 14–21.
[20] L. Schumacher and B. Dijkstra, "Description of a MATLAB implementation of the Indoor MIMO WLAN channel model proposed by the IEEE 802.11 TGn Channel Model Special Committee," Implementation note version 3.2 – May 2004. Available: http://www.info.fundp.ac.be/~lsc/Research/IEEE_80211_HTSG_CMSC/distribution_terms.html
[21] J. Ha et al., "LDPC Coded OFDM with Alamouti/SVD Diversity Technique," *Wireless Personal Communications*, vol. 23, no. 1, pp. 183–194, Oct. 2002.
[22] S. Haykin, "*Adaptive Filter Theory*," Englewood Cliffs, NJ: Prentice Hall, 1996.
[23] M. Clark, "IEEE 802.11a WLAN model," Mathworks, Inc., June 2003. Available: http://www.mathworks.com/matlabcentral/fileexchange/loadFile.do?objectId=3540&objectType=file
[24] T. Feist, "Rapid prototyping and verification of MIMO systems," *DSP Magazine*, May 2006.
[25] "*The Next Generation of Wireless Solutions*," Xilinx, Inc. Available: http://www.xilinx.com
[26] W. Sun and N. Trivedi, "Bluetooth, Wi-Fi: No Brawl over 2.4 GHz," *EE Times Asia*, Oct. 2007.
[27] O. Eliezer and M. Shoemake, "Bluetooth and Wi-Fi coexistence schemes strive to avoid chaos," *RF Design Magazine*, Nov. 2001.
[28] J. Andrews, A. Ghosh, and R. Muhamed, "*Fundamentals of WiMAX*," Pearson, New Jersey, 2007.
[29] A. Ghosh, D. Wolter, J. Andrews, and R. Chen, "Broadband Wireless Access with WiMAX/802.16: Current Performance Benchmarks and Future Potential," *IEEE Communications Magazine*, Feb. 2005.
[30] T. Paul, "A Study of Proposals for the IEEE 802.11n Wireless Local-Area Network Standard," MSEE Thesis, Santa Clara University, Dec. 2007

Thomas K. Paul (M'06) has worked in the communications industry since 1996. Most recently, he worked at Atheros Communications on the development of Wi-Fi phone products. Prior to that, at Ralink Technology, he worked on development of a cost-reduced version of the 802.11b WLAN chipset. Earlier, at PC-TEL Inc., he worked on the maintenance and improvement of their V.92 software modem product, attaining the position of Project Lead - Product Enhancement. He also holds a U.S. Patent regarding dynamic block processing in software modems. He earned the B.A.Sc. degree at the University of Toronto, Canada in 1996, and the M.S.E.E. at Santa Clara University, Santa Clara, California in 2007. His research interests are in communications system design and digital signal processing.

Tokunbo Ogunfunmi (M'88-SM'00) is currently an Associate Professor of Electrical Engineering and Director of the Signal Processing Research Lab (SPRL) at Santa Clara University (SCU), Santa Clara, California. From June-Nov., 2003 he served as Acting Chair, Electrical Engineering Dept., Santa Clara University. At SCU, he teaches a variety of courses in signal processing and related areas. His research interests include adaptive and nonlinear signal processing, artificial neural networks, signal processing for communications applications, multimedia and VLSI design. He has published one book and over 90 refereed journal and conference papers in these areas. Dr. Ogunfunmi has been a consultant to industry and government, and was a visiting professor at The University of Texas and at Stanford University. His industrial experiences include consulting for companies such as Broadcom, AMD, CASE Technology, CLARIS Corp., Clairvoyant, NEC, AT\&T Bell Labs. and NIKON Precision Research & Development.

He is a Senior Member of the Institution of Electrical and Electronic Engineers (IEEE), a Member of Sigma Xi (the Scientific Research Society) , and Member of the American Association for the Advancement of Science (AAAS). Previously he was Vice-Chair and is currently the Chair of the IEEE Signal Processing Society (SPS) Santa Clara Valley Chapter. He is also a member of the IEEE Circuits and Systems Society Technical Committee on Digital Signal Processing (DSP) and the IEEE Circuits and Systems Society Technical Committee on Circuits and Systems for Communications (CASCOM). He is also a registered professional engineer in California. Dr. Ogunfunmi received the Ph.D. in Electrical Engineering from Stanford University .